J. Fluid Mech. (2001), *vol.* 445, *pp.* 1–36. © 2001 Cambridge University Press
DOI: 10.1017/S0022112001005067 Printed in the United Kingdom

Three-dimensional natural convective states in a narrow-gap horizontal annulus

By MARK P. DYKO[1] AND KAMBIZ VAFAI[2]

[1]Department of Mechanical Engineering, The Ohio State University, Columbus, OH 43210, USA

[2]Department of Mechanical Engineering, University of California, Riverside, CA 92521, USA
e-mail: vafai@engr.ugr.edu

(Received 19 July 2000 and in revised form 9 February 2001)

Buoyancy-driven flow in a narrow-gap annulus formed by two concentric horizontal cylinders is investigated numerically. The three-dimensional transient equations of fluid motion and heat transfer are solved to study multiple supercritical states occurring within annuli having impermeable endwalls, which are encountered in various applications. For the first time, three-dimensional supercritical states are shown to occur in a narrow-gap annulus and the existence of four such states is established. These four states are characterized by the orientations and directions of rotation of counter-rotating rolls that form in the upper part of the annulus owing to thermal instability, and exhibit (i) transverse rolls, (ii) transverse rolls with reversed directions of rotation, (iii) longitudinal rolls in combination with transverse rolls, and (iv) longitudinal rolls with reversed directions of rotation in combination with transverse rolls, respectively. Simulations are performed at Rayleigh numbers approaching and exceeding the critical value to gain insight into the physical processes influencing development of the secondary flow structures. The evolution of the supercritical flow fields and temperature distributions with increasing Rayleigh number and the interaction between the secondary and primary flows are thoroughly investigated. Factors influencing the number of rolls are studied for each supercritical state. Heat transfer results are presented in the form of local Nusselt number distributions and overall annulus Nusselt numbers. Two-dimensional natural convection occurring early in the transient evolution of the flow field is also examined. Results obtained for a wide range of annulus radius ratios and Rayleigh numbers are shown to be in excellent agreement with results from previous experimental and numerical studies, thereby validating the present numerical scheme.

1. Introduction

Natural convection in the annular region between concentric cylinders has been extensively studied because of its many technological applications such as solar receivers, electrical transmission cables, nuclear reactors, cooling of electronic equipment, and aircraft brakes. Depending on the outer to inner cylinder radius ratio R and the Rayleigh number, various types of laminar flow structures can arise in the core region of a sufficiently long horizontal annulus. These structures were identified in some of the earlier experimental treatments of the problem using air as the working fluid. At lower Rayleigh numbers for a two-dimensional flow field, Liu, Mueller & Landis (1961) observed a unicellular flow with nearly stagnant regions at the top and

bottom of the annulus for small R. As the Rayleigh number was increased above a critical value, multiple counter-rotating cells arose in the upper portion of the annulus. With further increase in Rayleigh number, the angular extent of the cells became greater. In flow and temperature field visualization experiments performed by Grigull & Hauf (1966), a three-dimensional spiral type of fluid motion was found to emerge in the upper region of an annulus of moderate R at increased Rayleigh number. Using photographic techniques, Bishop & Carley (1966) identified two types of unicellular flow which set up in horizontal annuli at lower Rayleigh numbers. For R up to 2.45, a crescent-shaped flow pattern was observed, whereas a kidney-shaped pattern appeared for the largest R studied of 3.69. Powe, Carley & Bishop (1969) conducted experiments for a wide range of R. Based on their results and those of prior investigators, they classified various types of laminar natural convective regimes in horizontal cylindrical annuli as (i) a unicellular steady regime for small Rayleigh numbers at any value of R, (ii) a multicellular regime for higher Rayleigh numbers and $R < 1.24$ (narrow-gap annulus), (iii) a spiral flow regime for higher Rayleigh numbers and R between 1.24 and 1.71 (moderate-gap annulus), and (iv) an oscillating regime for higher Rayleigh numbers and $R > 1.71$ (large-gap annulus). Our results for narrow-gap annuli and the results obtained by Dyko, Vafai & Mojtabi (1999) for moderate- and large-gap annuli are consistent with the classifications by Powe *et al.* (1969). The occurrence of cellular instabilities in the nearly horizontal fluid layer formed locally by the upper part of a narrow-gap annulus is clearly demonstrated in the experimental studies and the present work. It was shown in the stability analysis of natural convective flow in narrow-gap annuli conducted by Walton (1980) that $Pr = 0.24$, which is less than that of air, is the critical value of the Prandtl number. For $Pr > 0.24$, the inception of instability occurs at the top of the annulus and is therefore thermal in nature, whereas for $Pr < 0.24$, it can arise elsewhere, indicating that it is partially hydrodynamic in origin.

Most of the prior studies of buoyancy-induced convection between horizontal concentric cylinders have dealt with two-dimensional flow in annuli with large length to gap-thickness ratios. There are relatively few studies of three-dimensional flow, which arises owing to the presence of the endwalls or the onset of instabilities at higher Rayleigh numbers. Previous numerical investigations of three-dimensional natural convection in large-gap annuli have focused on the effect of annulus inclination (Takata *et al.* 1984), flow patterns in a very short annulus (Fusegi & Farouk 1986), transient formation of the flow and temperature fields (Vafai & Ettefagh 1991), turbulent flow (Desai & Vafai 1994), and high-Rayleigh-number laminar flow for air and larger-Prandtl-number fluids (Dyko *et al.* 1999). To our knowledge, only two numerical studies of three-dimensional supercritical flow in a horizontal annulus are available in the literature. Rao *et al.* (1985) analysed spiral natural convection in a moderate-gap annulus. They considered only a fluid with a Prandtl number of 5000, which limits the range of practical applicability of their results. Dyko *et al.* (1999) investigated the development of spiral flow in air-filled moderate-gap annuli, its interaction with the primary flow, and factors influencing the number and size of spiral vortex cells. There are no previously published studies of three-dimensional supercritical or subcritical natural convection in narrow-gap cylindrical annuli. It was therefore the aim of the present work to investigate three-dimensional natural convective flow structures and temperature fields in narrow-gap annuli at Rayleigh numbers approaching and exceeding the critical value Ra_c for thermal instability, including the effects of varying R and annulus length.

Experimental and numerical evidence in the literature indicates the presence of a

multiplicity of solutions (known as the bifurcation phenomenon) in natural convection problems which occurs at higher Rayleigh numbers and is related to thermal or hydrodynamic instability. In the limited two-dimensional numerical studies of natural convection in narrow-gap annuli containing air conducted previously, two or more solutions are shown to occur for a given combination of R and supercritical Rayleigh number, depending on initial conditions. Only two-dimensional models were employed in these studies and therefore neither three-dimensional supercritical flows nor the effects of solid endwalls could be analysed. Rao *et al.* (1985) analysed flow patterns of buoyancy-induced convection in air-filled narrow-gap annuli. They calculated a steady multicellular flow for a Rayleigh number immediately above the critical value, which changed to an oscillatory flow as the Rayleigh number was increased to higher values. Fant, Rothmeyer & Prusa (1991) obtained steady bicellular and tricellular solutions for $R = 1.2$ and $R = 1.1$, respectively. Kim & Ro (1994) extended the results for $R = 1.2$ to include the tricelluar bifurcating solution, and Yoo (1996) later confirmed the bicellular and tricellular solutions for $R = 1.2$. A two-dimensional analysis of multicellular natural convective flow of air in narrow-gap annuli was also performed by Cadiou, Desrayoud & Lauriat (1998). They calculated two branches of supercritical solutions corresponding to an upward and downward radial velocity, respectively, at the upper vertical centreline (opposite directions of cell rotation). At very high Rayleigh numbers, secondary shear-driven instabilities were found to appear within the crescent base flow for $R < 1.15$. Chung *et al.* (1999) obtained a tetracellular solution at very high Rayleigh numbers for $R = 1.2$. A few authors have studied natural convection in narrow-gap annuli numerically for very small Prandtl numbers or the limiting case of zero Prandtl number (Fant *et al.* 1990, 1991; Yoo, Choi & Kim 1994). For these cases, hydrodynamic-type instabilities originate in the two side regions of the annulus, similar to natural convection in a vertical cavity of large aspect ratio.

In the present work, three-dimensional natural convection in a narrow-gap annulus with solid endwalls is investigated for the first time. Multiple supercritical states exhibiting either transverse rolls (axes of the rolls oriented in the angular direction) in the upper portion of the annulus or longitudinal rolls (axes parallel to the common axis of the inner and outer cylinders) in the highest part of the annulus in combination with transverse rolls located between the longitudinal rolls and primary flow (seen as a crescent-shaped recirculation pattern on each side of the annulus when viewed in any axial plane) are studied. Owing to the presence of the transverse rolls, none of these states can be simulated using a two-dimensional model. The governing equations are formulated in terms of vorticity and vector potential. The parabolic equations are solved by a three-dimensional three-level time-splitting ADI method and the elliptic equations are solved by the extrapolated Jacobi scheme. Three-dimensional numerical solutions for a wide range of annulus radius ratios and Rayleigh numbers as well as different Prandtl numbers are shown to be in excellent agreement with results from previous experimental and numerical studies. The manifestation of thermal instability as the formation of three-dimensional secondary flows and the effects of Rayleigh number and annulus geometry on the flow and temperature fields are elucidated.

2. Problem formulation and solution

A fluid layer is bounded by two concentric horizontal cylinders of length l with inner and outer radii r_i and r_o respectively, and two vertical endwalls. The temperature of the inner cylinder is greater than that of the outer cylinder ($T_i > T_o$) and the endwalls

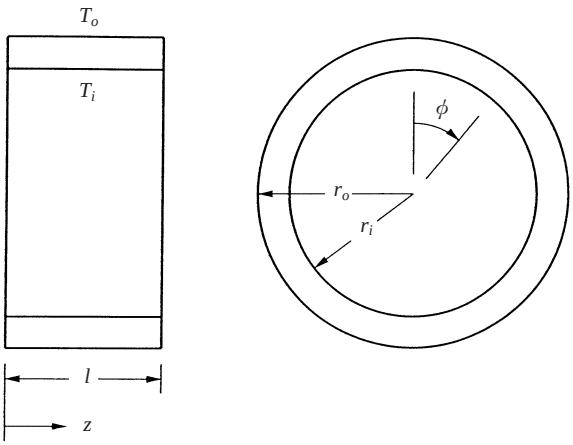

FIGURE 1. Geometry and coordinate system.

are impermeable and adiabatic. The non-dimensional radius ratio $R = r_o/r_i$ and gap aspect ratio $A = l/(r_o - r_i)$ are used to characterize the narrow gap annulus geometry, which is illustrated in figure 1. The dimensionless axial length is defined by $L = l/r_i$. As shown in figure 1, a cylindrical coordinate system (r, ϕ, z) is employed where the angular coordinate ϕ is measured with reference to the upward vertical. The computational domain was chosen to encompass the full radial ($1 \leqslant r \leqslant R$), angular ($-\pi \leqslant \phi \leqslant \pi$), and axial ($0 \leqslant z \leqslant L$) extent of the annulus for all of the numerical simulations.

2.1. *Governing equations*

The non-dimensional governing equations of transient, three-dimensional, laminar, buoyancy-induced flow of an incompressible, Newtonian fluid using the Boussinesq approximation are

$$\nabla \cdot \boldsymbol{V} = 0, \tag{1}$$

$$\frac{\partial \boldsymbol{V}}{\partial t} + (\boldsymbol{V} \cdot \nabla)\boldsymbol{V} = -\nabla P + Pr\nabla^2 \boldsymbol{V} - PrRa_r \boldsymbol{k}\Theta, \tag{2}$$

$$\frac{\partial \Theta}{\partial t} + (\boldsymbol{V} \cdot \nabla)\Theta = \nabla^2 \Theta, \tag{3}$$

where $\boldsymbol{k} = -\cos\phi\, \boldsymbol{e}_1 + \sin\phi\, \boldsymbol{e}_2$ is a unit vector in the direction of the gravitational force and $\boldsymbol{e}_1$, $\boldsymbol{e}_2$ and $\boldsymbol{e}_3$ are the unit vectors in the r, ϕ and z directions, respectively. The above equations are non-dimensionalized using the scaling factors r_i for length, α/r_i for velocity, r_i^2/α for time and $\rho\alpha^2/r_i^2$ for pressure, with α and ρ denoting the thermal diffusivity and density, respectively. The dimensionless temperature is defined by $\Theta = (T - T_o)/\Delta T$, where $\Delta T = T_i - T_o$, and the dimensionless parameters, Rayleigh number Ra_r and Prandtl number Pr, are defined as

$$Ra_r = \frac{g\beta r_i^3 \Delta T}{\alpha v}, \quad Pr = \frac{v}{\alpha}, \tag{4}$$

where g is the acceleration due to gravity, β the coefficient of thermal expansion, and v the kinematic viscosity. The Rayleigh number based on annular gap width $r_o - r_i$, which is employed later to facilitate comparison of the results to those from previous

studies, is defined as

$$Ra = \frac{g\beta(r_o - r_i)^3 \Delta T}{\alpha v}. \tag{5}$$

The pressure term is eliminated by taking the curl of the momentum equation (2), which yields the dimensionless vorticity transport equations

$$\frac{\partial \Omega_r}{\partial t} + V_r \frac{\partial \Omega_r}{\partial r} + \frac{V_\phi}{r}\frac{\partial \Omega_r}{\partial \phi} + V_z \frac{\partial \Omega_r}{\partial z} - \Omega_r \frac{\partial V_r}{\partial r} - \frac{\Omega_\phi}{r}\frac{\partial V_r}{\partial \phi} - \Omega_z \frac{\partial V_r}{\partial z}$$
$$= Pr\left(\frac{1}{r}\frac{\partial \Omega_r}{\partial r} + \frac{\partial^2 \Omega_r}{\partial r^2} + \frac{1}{r^2}\frac{\partial^2 \Omega_r}{\partial \phi^2} + \frac{\partial^2 \Omega_r}{\partial z^2} - \frac{\Omega_r}{r^2} - \frac{2}{r^2}\frac{\partial \Omega_\phi}{\partial \phi}\right) + PrRa_r \sin\phi \frac{\partial \Theta}{\partial z}, \tag{6}$$

$$\frac{\partial \Omega_\phi}{\partial t} + V_r \frac{\partial \Omega_\phi}{\partial r} + \frac{V_\phi}{r}\frac{\partial \Omega_\phi}{\partial \phi} + V_z \frac{\partial \Omega_\phi}{\partial z} - \Omega_r \frac{\partial V_\phi}{\partial r} - \frac{\Omega_\phi}{r}\frac{\partial V_\phi}{\partial \phi} - \Omega_z \frac{\partial V_\phi}{\partial z} + \frac{V_\phi \Omega_r - V_r \Omega_\phi}{r}$$
$$= Pr\left(\frac{1}{r}\frac{\partial \Omega_\phi}{\partial r} + \frac{\partial^2 \Omega_\phi}{\partial r^2} + \frac{1}{r^2}\frac{\partial^2 \Omega_\phi}{\partial \phi^2} + \frac{\partial^2 \Omega_\phi}{\partial z^2} - \frac{\Omega_\phi}{r^2} + \frac{2}{r^2}\frac{\partial \Omega_r}{\partial \phi}\right) + PrRa_r \cos\phi \frac{\partial \Theta}{\partial z}, \tag{7}$$

$$\frac{\partial \Omega_z}{\partial t} + V_r \frac{\partial \Omega_z}{\partial r} + \frac{V_\phi}{r}\frac{\partial \Omega_z}{\partial \phi} + V_z \frac{\partial \Omega_z}{\partial z} - \Omega_r \frac{\partial V_z}{\partial r} - \frac{\Omega_\phi}{r}\frac{\partial V_z}{\partial \phi} - \Omega_z \frac{\partial V_z}{\partial z}$$
$$= Pr\left(\frac{1}{r}\frac{\partial \Omega_z}{\partial r} + \frac{\partial^2 \Omega_z}{\partial r^2} + \frac{1}{r^2}\frac{\partial^2 \Omega_z}{\partial \phi^2} + \frac{\partial^2 \Omega_z}{\partial z^2}\right) - PrRa_r\left(\sin\phi \frac{\partial \Theta}{\partial r} + \frac{1}{r}\cos\phi \frac{\partial \Theta}{\partial \phi}\right), \tag{8}$$

where the vorticity vector is defined by $\boldsymbol{\Omega} = \nabla \times \boldsymbol{V}$.

The vector potential $\boldsymbol{\Psi}$ is introduced, where $\boldsymbol{V} = \nabla \times \boldsymbol{\Psi}$. Note that the continuity equation (1) is satisfied automatically by this expression. Imposing the solenoidal condition $\nabla \cdot \boldsymbol{\Psi} = 0$, the following equations relating vector potential and vorticity are obtained

$$\frac{1}{r}\frac{\partial \Psi_r}{\partial r} + \frac{\partial^2 \Psi_r}{\partial r^2} + \frac{1}{r^2}\frac{\partial^2 \Psi_r}{\partial \phi^2} + \frac{\partial^2 \Psi_r}{\partial z^2} + \frac{2}{r}\frac{\partial \Psi_r}{\partial r} + \frac{\Psi_r}{r^2} + \frac{2}{r}\frac{\partial \Psi_z}{\partial z} = -\Omega_r, \tag{9}$$

$$\frac{1}{r}\frac{\partial \Psi_\phi}{\partial r} + \frac{\partial^2 \Psi_\phi}{\partial r^2} + \frac{1}{r^2}\frac{\partial^2 \Psi_\phi}{\partial \phi^2} + \frac{\partial^2 \Psi_\phi}{\partial z^2} - \frac{\Psi_\phi}{r^2} + \frac{2}{r^2}\frac{\partial \Psi_r}{\partial \phi} = -\Omega_\phi, \tag{10}$$

$$\frac{1}{r}\frac{\partial \Psi_z}{\partial r} + \frac{\partial^2 \Psi_z}{\partial r^2} + \frac{1}{r^2}\frac{\partial^2 \Psi_z}{\partial \phi^2} + \frac{\partial^2 \Psi_z}{\partial z^2} = -\Omega_z. \tag{11}$$

From the definition of vector potential, the components of dimensionless velocity are

$$V_r = \frac{1}{r}\frac{\partial \Psi_z}{\partial \phi} - \frac{\partial \Psi_\phi}{\partial z}, \tag{12}$$

$$V_\phi = \frac{\partial \Psi_r}{\partial z} - \frac{\partial \Psi_z}{\partial r}, \tag{13}$$

$$V_z = \frac{\Psi_\phi}{r} + \frac{\partial \Psi_\phi}{\partial r} - \frac{1}{r}\frac{\partial \Psi_r}{\partial \phi}. \tag{14}$$

The energy equation (3) is written in final form as

$$\frac{\partial \Theta}{\partial t} + V_r \frac{\partial \Theta}{\partial r} + \frac{V_\phi}{r}\frac{\partial \Theta}{\partial \phi} + V_z \frac{\partial \Theta}{\partial z} = \frac{1}{r}\frac{\partial \Theta}{\partial r} + \frac{\partial^2 \Theta}{\partial r^2} + \frac{1}{r^2}\frac{\partial^2 \Theta}{\partial \phi^2} + \frac{\partial^2 \Theta}{\partial z^2}. \tag{15}$$

Equations (6)–(15) are the final form of the non-dimensional governing equations

which comprise a system of ten coupled partial differential equations for ten unknowns: Ω_r, Ω_ϕ, Ω_z, Ψ_r, Ψ_ϕ, Ψ_z, V_r, V_ϕ, V_z, and Θ.

2.2. *Boundary and initial conditions*

The temperatures of the annulus inner and outer cylinders are maintained at $\Theta = 1$ and $\Theta = 0$, respectively. The components of velocity are zero at the cylinder surfaces, and the components of vorticity are obtained from $\boldsymbol{\Omega} = \nabla \times \boldsymbol{V}$. The vector potential boundary conditions are consistent with the work of Hirasaki & Hellums (1968), with the normal gradient of the normal component of vector potential and the components of vector potential tangential to the surface specified as zero. Therefore, the dimensionless boundary conditions at $r = 1$ and $r = R$ (over $-\pi < \phi < \pi$ and $0 < z < L$) are as follows

$$\Theta = 1 \quad \text{at} \quad r = 1, \tag{16}$$

$$\Theta = 0 \quad \text{at} \quad r = R, \tag{17}$$

$$V_r = V_\phi = V_z = 0 \quad \text{at} \quad r = 1, R, \tag{18}$$

$$\Omega_r = 0, \quad \Omega_\phi = -\frac{\partial V_z}{\partial r}, \quad \Omega_z = \frac{\partial V_\phi}{\partial r} \quad \text{at} \quad r = 1, R, \tag{19}$$

$$\frac{\partial}{\partial r}(r\Psi_r) = \Psi_\phi = \Psi_z = 0 \quad \text{at} \quad r = 1, R. \tag{20}$$

All of the numerical simulations were performed over the full radial, angular, and axial extent of the annulus. Simulations were first conducted using periodic boundary conditions at the lower vertical angular plane $\phi = \pi(-\pi)$ (to join the computational domain) to rigorously demonstrate that the flow is symmetric about this plane for the ranges of R, A, and Rayleigh number investigated. In subsequent numerical simulations within these ranges, symmetry boundary conditions (equations (21)–(24)) were employed only at $\phi = \pi(-\pi)$ (over $1 < r < R$ and $0 < z < L$) for enhanced computational efficiency. Note that the simulations with periodic boundary conditions at $\phi = \pi(-\pi)$ were compared to the corresponding cases with symmetry boundary conditions at $\phi = \pi(-\pi)$ and the results were found to be identical.

$$\frac{\partial \Theta}{\partial \phi} = 0 \quad \text{at} \quad \phi = \pi(-\pi), \tag{21}$$

$$\frac{\partial V_r}{\partial \phi} = V_\phi = \frac{\partial V_z}{\partial \phi} = 0 \quad \text{at} \quad \phi = \pi(-\pi), \tag{22}$$

$$\Omega_r = \frac{\partial \Omega_\phi}{\partial \phi} = \Omega_z = 0 \quad \text{at} \quad \phi = \pi(-\pi), \tag{23}$$

$$\Psi_r = \frac{\partial \Psi_\phi}{\partial \phi} = \Psi_z = 0 \quad \text{at} \quad \phi = \pi(-\pi). \tag{24}$$

At the adiabatic endwalls of the annulus, the normal gradient of temperature and the three components of velocity are zero. Therefore, the boundary conditions at $z = 0$ and $z = L$ (over $1 < r < R$ and $-\pi < \phi < \pi$) are

$$\frac{\partial \Theta}{\partial z} = 0 \quad \text{at} \quad z = 0, L, \tag{25}$$

$$V_r = V_\phi = V_z = 0 \quad \text{at} \quad z = 0, L, \tag{26}$$

$$\Omega_r = -\frac{\partial V_\phi}{\partial z}, \quad \Omega_\phi = \frac{\partial V_r}{\partial z}, \quad \Omega_z = 0 \quad \text{at} \quad z = 0, L, \tag{27}$$

$$\Psi_r = \Psi_\phi = \frac{\partial \Psi_z}{\partial z} = 0 \quad \text{at} \quad z = 0, L. \tag{28}$$

In previous two-dimensional numerical studies dealing with bifurcative natural convection of air in long horizontal annuli, various types of initial conditions were employed to obtain multiple supercritical solutions corresponding to different directions of rotation and numbers of longitudinally oriented rolls. Usually, one multicellular solution was achieved by successively increasing the Rayleigh number starting from a subcritical value and using each solution as the initial condition for the next higher Rayleigh number. A second multicellular solution with reversed directions of cell rotation was obtained using another set of initial conditions such as a motionless state with either a uniform or perturbed temperature field, and abruptly increasing the Rayleigh number to a value greater than Ra_c. Cadiou *et al.* (1998) showed that these two types of solutions bifurcate from the unicellular flow at $Ra = Ra_c$. At Rayleigh numbers much greater than Ra_c, a solution exhibiting a greater number of cells was obtained by Chung *et al.* (1999) using specialized initial conditions.

A total of four three-dimensional supercritical states are investigated in the present study. One state is obtained by successively increasing the Rayleigh number from subcritical to supercritical values. In this case, transverse end rolls that carry over from the subcritical solution determine the orientation and directions of rotation of supercritical rolls that subsequently form in the annulus, as explained in § 3.1. These end rolls also develop prior to the formation of supercritical rolls when starting from quiescent and isothermal initial conditions, resulting in the same supercritical state. In order for the other three states to arise, the supercritical rolls must be induced to form prior to the development of the end rolls. To accomplish this, perturbed conductive temperature fields of the same general type as that employed by Cheddadi *et al.* (1992) to induce cellular flow are used as initial conditions in the present study. These perturbed temperature fields, which are presented in equations (29) and (30), physically simulate the reversal of thermal gradients associated with inception of thermal instabilities in the annulus. Equation (29) is periodic in the axial direction and consequently triggers formation of transverse rolls, while equation (30) is periodic in the angular direction and leads to the development of longitudinal rolls. In these equations, C_A is an amplification coefficient, C_B is the wavenumber, and η is the phase shift of the temperature perturbation.

$$\Theta = 1 - (\ln r / \ln R) + C_A \sin(\pi \ln r / \ln R)(-\cos(C_B \pi z + \eta)), \tag{29}$$

$$\Theta = 1 - (\ln r / \ln R) + C_A \sin(\pi \ln r / \ln R)\cos(C_B \phi + \eta). \tag{30}$$

2.3. *Solution procedure*

The three-dimensional governing equations (6)–(15) are solved in conjunction with the boundary conditions (16)–(28) using a finite-difference method. A modified form of the three-dimensional alternating direction implicit (ADI) method developed by Brian (1961) is employed to advance the energy equation (15) and vorticity equations (6)–(8) in time. The vector potential equations (9)–(11) are solved iteratively within each timestep using the extrapolated Jacobi scheme with optimum over-relaxation. Velocities are evaluated using central difference approximations to equations (12)–(14). At each time level, convergence to steady state is checked by calculating the relative

changes of the temperature, vorticity components, and vector potential components at every grid point and comparing these to a prescribed constant, which was set to 10^{-3}. Steady state is assumed to have been achieved when

$$\frac{\xi^{n+1}_{i,j,k} - \xi^{n}_{i,j,k}}{\xi^{n}_{i,j,k}} \leqslant 10^{-3}, \tag{31}$$

where n is a particular time level and ξ is any one of the dependent variables.

In order to properly capture the counter-rotating rolls that arise at the top of the annulus owing to thermal instabilities, a very fine grid distribution is used in this region. A non-uniform grid size in the angular direction is employed in order to minimize the total number of grids without sacrificing accuracy, with the larger size grids located in the lower portion of the annulus where angular gradients of the temperature and flow variables are smaller. The spatial derivatives in the non-uniform grid system are approximated by the following central difference expressions

$$\left.\frac{\partial f}{\partial \phi}\right|_{i,j,k} = \frac{f_{i,j+1,k} - f_{i,j-1,k}}{\Delta\phi_{j-1} + \Delta\phi_j}, \tag{32}$$

$$\left.\frac{\partial^2 f}{\partial \phi^2}\right|_{i,j,k} = \frac{2\Delta\phi_{j-1} f_{i,j+1,k} - 2(\Delta\phi_{j-1} + \Delta\phi_j) f_{i,j,k} + 2\Delta\phi_j f_{i,j-1,k}}{\Delta\phi_{j-1}\Delta\phi_j(\Delta\phi_{j-1} + \Delta\phi_j)}, \tag{33}$$

where $\Delta\phi_{j-1}$ is the angular distance between grid points i, j, k and i, $j-1$, k, and $\Delta\phi_j$ is the angular distance between grid points i, $j+1$, k and i, j, k. The change in grid size in the transition region between the fine mesh at the top of the annulus and the coarser mesh in the lower portion is chosen such that

$$\Delta\phi_j - \Delta\phi_{j-1} \cong O(\Delta\phi^2_{j-1}). \tag{34}$$

This criterion ensures that use of equations (32) and (33) results in a local truncation error that is of the same order of magnitude as would occur in a uniformly spaced system. By gradually changing the grid size in this manner, the extra reduction in accuracy that would otherwise occur at the boundary between regions of different grid size is avoided. An example of radial, angular, and axial grid distributions showing the fine, transition, and coarse angular mesh regions is provided in figure 2.

2.4. *Heat transfer calculations*

The inner and outer cylinder mean Nusselt numbers are the spatial averages of the local Nusselt number over the inner and outer cylinders, respectively, where the local Nusselt number is the ratio of the actual to conduction heat transfer. The expressions for the inner and outer cylinder mean Nusselt numbers $\overline{Nu}_i$ and $\overline{Nu}_o$, respectively, are

$$\overline{Nu}_i = \frac{-1}{2\pi L}\int_0^L \int_0^{2\pi} \ln(R) \left.\frac{\partial \Theta}{\partial r}\right|_{r=1} \mathrm{d}\phi\, \mathrm{d}z, \tag{35}$$

$$\overline{Nu}_o = \frac{-1}{2\pi L}\int_0^L \int_0^{2\pi} R\, \ln(R) \left.\frac{\partial \Theta}{\partial r}\right|_{r=R} \mathrm{d}\phi\, \mathrm{d}z. \tag{36}$$

At steady state conditions, $\overline{Nu}_i$ and $\overline{Nu}_o$ converge to the same value, which is reported herein as the overall annulus Nusselt number. This fact was used as a further check on the accuracy of the numerical scheme.

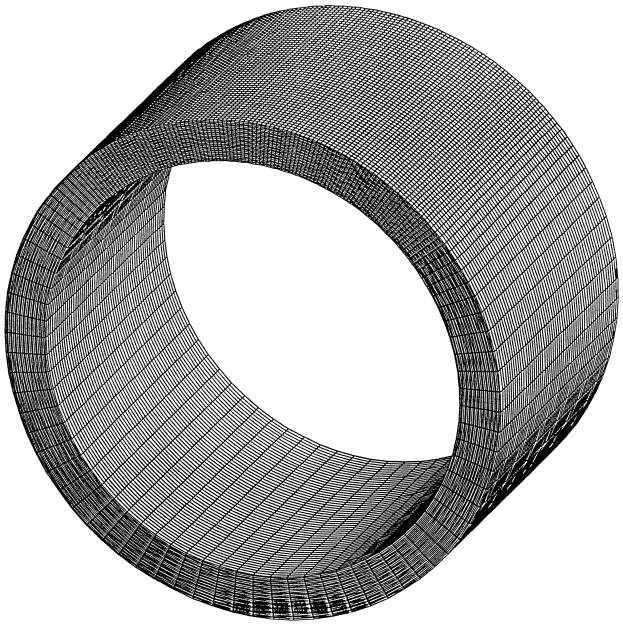

FIGURE 2. Example of radial, angular, and axial grid distributions used in the computations.

3. Results and discussion

The development of flow patterns and temperature distributions as the Rayleigh number is successively increased from subcritical to supercritical values is presented. Multiple three-dimensional supercritical states characterized by the orientations and directions of rotation of convective rolls that form in the upper region of the annulus owing to thermal instability are analysed, and factors influencing the number of supercritical rolls are studied. A critical Rayleigh number above which the basic flow is unstable is determined from the numerical results.

As indicated earlier, all of the numerical simulations were performed over the full angular and axial extent of the annulus. It was demonstrated that, owing to flow symmetry, the normal component of velocity and normal gradients of the tangential velocity components are zero at the vertical angular plane and the mid-axial plane. Accordingly, the ϕ-component of vector potential corresponds to the two-dimensional stream function at the vertical angular plane, and the z-component of vector potential corresponds to the two-dimensional stream function at the mid-axial plane. In § 3.1, supercritical states exhibiting only transverse rolls in the upper part of the annulus are studied. In this case, results are presented as streamlines and isotherms at the upper vertical angular plane since these provide a characteristic cross-section of the flow and temperature fields associated with the transverse rolls. Supercritical states that display longitudinal rolls in the highest part of the annulus in combination with transverse rolls located between the longitudinal rolls and primary flow are studied in § 3.2. For this case, the streamlines and isotherms at the mid-axial plane provide a representative cross-section of the flow and temperature fields associated with the longitudinal rolls.

A systematic mesh refinement procedure was employed to ensure that the results are not dependent on grid size. In this procedure, the number of grid points in the radial, angular, and axial directions, and the angular boundaries of the fine mesh and

transition mesh regions were independently varied. The results of these runs were compared to determine the grid distribution which yielded grid-independent results. The number of grid points in the radial direction was first successively increased while the angular and axial grid points were held constant. Keeping the number of axial grid points the same and using the grid size in the radial direction obtained from the previous step, the angular boundaries of the fine mesh and transition mesh regions were then successively increased to ensure that the rolls that form in the upper portion of the annulus were properly captured. Once the boundaries of the angular mesh regions were determined, the number of grid points in the angular direction was successively increased. With the angular and radial grid sizes thus established, the number of grid points in the axial direction was then successively increased. Finally, the number of grid points in all three directions as well as the angular boundaries of the fine mesh and transition mesh regions were increased to determine the grid distribution which yielded grid-independent results. Note that the ratio of adjacent grid sizes in the transition mesh region was always set to satisfy the equation (34) criterion.

The mesh refinement procedure was conducted over the ranges of R and Rayleigh number studied. The required number of angular grid points was found to vary with both R and Rayleigh number. As expected, the greatest number of angular grids is associated with the smallest R at the highest Rayleigh number. Also, the required angular extent of the fine mesh region varies depending on the Rayleigh number, with the largest angular extent corresponding to the highest Rayleigh number. For gap aspect ratios greater or less than the baseline value of $A = 7$, the number of axial grid points was increased or decreased, respectively, according to the aspect ratio.

Sufficiently small timesteps in the range of 10^{-5} to 10^{-6} were used to obtain timestep-independent solutions. In separate numerical runs, the timestep was initially set to a large value and then progressively decreased until the transient solution no longer changed. Following this procedure, the step size which yielded timestep-independent results was determined for each case studied.

In addition to the studies performed to ensure grid- and timestep-independence, steady state results were compared to those of previous numerical and experimental investigations to verify the accuracy of the numerical scheme. These comparisons are presented in Dyko *et al.* (1999), and thus are only summarized briefly here. Four sets of comparisons were made, the first three for air as the fluid medium with Rayleigh numbers in the range of $Ra = 10^3$ to 1.1×10^4, and the fourth for a fluid with $Pr = 100$ and Rayleigh numbers of $Ra = 8.725 \times 10^3$ and 2.52×10^4. The results of these comparisons show that the streamlines and isotherms calculated using the present numerical scheme are in excellent agreement with the experimental results of Dyko *et al.* (1999) for air and a fluid with $Pr = 100$, as well as the numerical results of Kuehn & Goldstein (1976) for air. In addition, other important features of the natural convective flows such as the position and size of transverse vortex structures, centre of rotation of unicellular flows, and movement of the centre of rotation with increasing Rayleigh number are seen to be properly captured by the numerical model.

For further verification of the numerical algorithm employed in the present investigation, comparisons were made between longitudinal rolls that set up early in the transient evolution of the three-dimensional flow field, and the steady counter-rotating cells obtained by Cadiou *et al.* (1998) using a two-dimensional model for the case of $R = 1.04$, $Ra = 3000$, and $Pr = 0.7$. These comparisons are valid since the flow in the mid-axial region of the annulus remains two-dimensional until a later time when adjoining transverse rolls begin to form there. In figure 3, streamlines and

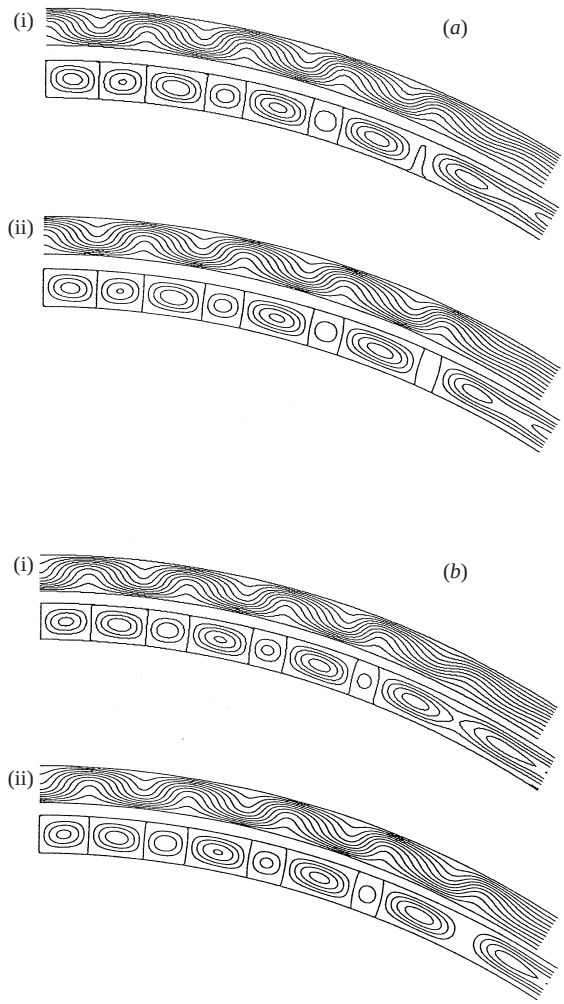

FIGURE 3. Comparisons of isotherms and streamlines occurring early in the transient evolution of the three-dimensional flow field at the mid-axial plane $z = \frac{1}{2}L$ (present work) to those obtained using a two-dimensional model (Cadiou *et al.* 1998) for $R = 1.04$, $Ra = 3000$, and $Pr = 0.7$: (*a*) first supercritical state; (i) Present Work: Cross-section (at $z = \frac{1}{2}L$) of three-dimensional longitudinal rolls very early in the transient development of the flow field ($t = 0.001$), prior to formation of the adjoining three-dimensional transverse rolls; (ii) Cadiou *et al.* (1998): Steady cells from a two-dimensional model (the two-dimensional model cannot simulate the adjoining three-dimensional transverse rolls that are actually present at steady state); (*b*) second supercritical state. (i) Present Work: Cross-section (at $z = \frac{1}{2}L$) of three-dimensional longitudinal rolls very early in the transient development of the flow field ($t = 0.001$), prior to formation of the adjoining three-dimensional transverse rolls; (ii) Cadiou *et al.* (1998): Steady cells from a two-dimensional model (the two-dimensional model cannot simulate the adjoining three-dimensional transverse rolls that are actually present at steady state).

isotherms from their work are plotted next to those at the mid-axial plane from the present three-dimensional study, for two different supercritical states. It is seen that the streamlines and isotherms in the upper part of the annulus from our numerical model are in excellent agreement with their solutions from the two branches of the bifurcation curve for two-dimensional flow. These two branches correspond to cells with

reversed directions of rotation. Note that since Cadiou *et al.*'s (1998) two-dimensional model cannot simulate the three-dimensional transverse rolls that are in place next to the longitudinal rolls at steady state, their steady results are incorrect. It should be noted that a two-dimensional simulation of the narrow-gap annulus cannot represent the three-dimensional transverse rolls that are indeed present at steady state.

3.1. *Transverse rolls*

Three-dimensional natural convective flow consisting of transverse rolls in the upper region of the annulus in conjunction with the primary recirculating flow outside this region is studied in this section. Simulations were conducted for an annulus of radius ratio $R = 1.1$ and gap aspect ratio $A = 7$, with air ($Pr = 0.7$) as the fluid medium. The Rayleigh number was successively increased from $Ra = 1000$ to $Ra = 3000$, which enabled investigation of subcritical and supercritical flow structures. To illustrate the effects of gap aspect ratio on the supercritical flow and temperature fields, results are presented for $A = 5$, 6 and 8. The results of simulations performed for $R = 1.05$, 1.15 and 1.2 to study the influence of radius ratio are also provided.

At a Rayleigh number of $Ra = 1000$, two crescent-shaped recirculation patterns centred on $\phi = \pm\frac{1}{2}\pi$ are present in each of the axial planes. These patterns are symmetric to one another about the vertical angular plane. The isotherms appear as concentric circles centred on $r = 0$ (when viewed in any axial plane) indicating that heat transfer takes place essentially by conduction only. When viewed in any of the (r, z)-planes, the isotherms form horizontal straight lines without any noticeable distortion near the endwalls. Note that, for conciseness, plots of the flow patterns and isotherms for $Ra = 1000$ are not presented.

When the Rayleigh number is increased to $Ra = 1500$, the temperature field retains its two-dimensional characteristics except in the upper region of the annulus near the endwalls. Here, the isotherms become slightly distorted owing to the increased strength of locally three-dimensional flow that results from the viscous shearing effect of the endwalls. As the Rayleigh number is increased above the critical value for instability of $Ra_c = 1740$ for $R = 1.1$ determined in the present study, the isotherms in the upper region begin to vary noticeably over the entire length of the annulus. As shown later, this is an indication of the formation of three-dimensional secondary flow structures in the upper region of the annulus. The heat transfer from the inner to outer cylinder begins to depart from that of pure conduction as a result of these secondary flows.

The streamlines and isotherms in the upper vertical angular plane are plotted in figures 4(*a*) and 4(*b*), respectively, for a Rayleigh number of $Ra = 1500$. At this subcritical Rayleigh number, a core region of approximately $\frac{1}{8}L < z < \frac{7}{8}L$ exists in which the temperature distribution is essentially independent of axial position and the axial velocity is very small. In figure 4(*a*) a rotational cell is seen to be present at each endwall. These cells are actually cross-sections of transverse rolls extending across the upper region that rotate clockwise and counterclockwise on the right- and left-hand sides of the annulus, respectively. The strength of these end rolls is very low, which results in only a slight distortion of the isotherms near the endwalls, as observed in figure 4(*b*). In figure 4(*a*), an even weaker counter-rotating secondary flow pattern produced by viscous shear forces is seen to be present next to each end roll. At this Rayleigh number, the overall Nusselt number is $Nu_{av} = 1.003$ which indicates that heat transfer occurs almost entirely by conduction.

As the Rayleigh number is increased above the critical value $Ra_c = 1740$, two additional pairs of counter-rotating cells form in the central space between the

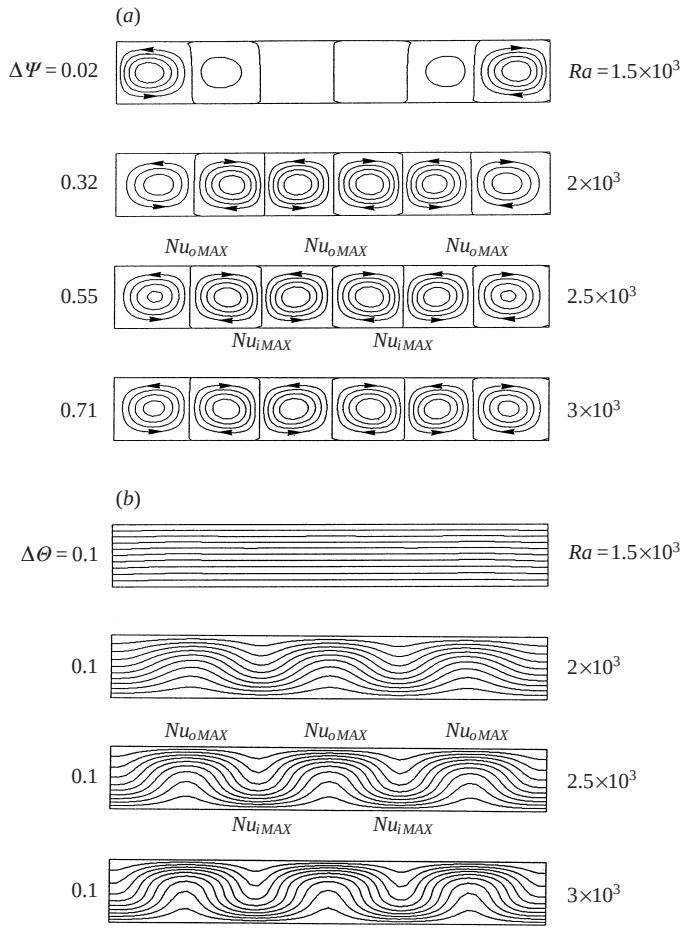

FIGURE 4. Effect of Ra on convection at the upper vertical angular plane for the first type of transverse roll pattern for $R = 1.1$, $A = 7$, $Pr = 0.7$: (a) streamlines; (b) isotherms.

end rolls, thereby eliminating the core region, as seen in figures 4(a) and 4(b) for $Ra = 2000$. Each of the cells is a cross-section of a transverse roll that arises owing to thermal instability. Note that at Rayleigh numbers slightly greater than $Ra_c = 1740$, the inner transverse rolls are weaker than the end rolls. However, as the Rayleigh number is increased, the strength of the inner rolls increases faster than that of the end rolls and becomes slightly greater prior to reaching $Ra = 1800$. As the Rayleigh number is elevated further, the end rolls remain weaker than the inner rolls because of the viscous shearing effect of the endwalls, as shown in figure 4(a) for $Ra = 2000$, 2500 and 3000. The strength of the supercritical inner rolls increases significantly with Rayleigh number, as seen by comparing the maximum values of stream function at the upper vertical angular plane of 0.69, 1.58, 2.77 and 3.57 for $Ra = 1800$, 2000, 2500 and 3000, respectively. At each Rayleigh number, the strength of each of the four inner rolls is almost the same.

The alternating elevation and depression of isotherms along the length of the annulus observed in figure 4(b) for Rayleigh numbers of $Ra = 2000$, 2500 and 3000 reflects the upward and downward movement of fluid corresponding to the opposing directions of rotation of the transverse rolls. The closer spacing of isotherms next

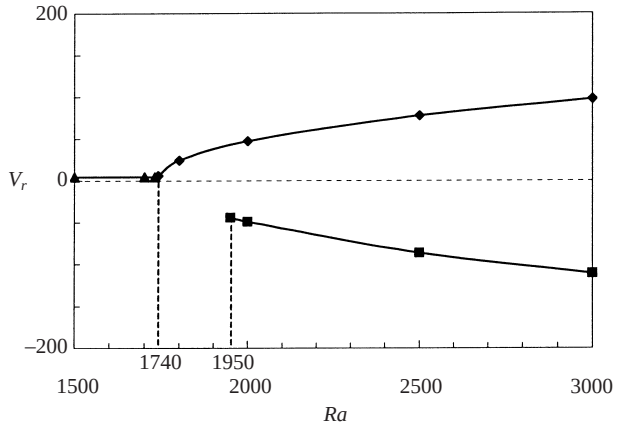

FIGURE 5. Radial velocity at $r = \frac{1}{2}(r_i + r_o)$, $\phi = 0$, $z = \frac{1}{2}L$ as a function of Rayleigh number for ◆, the first type of transverse rolls, ■, second type of transverse rolls, and ▲, subcritical flow for $R = 1.1$, $A = 7$, $Pr = 0.7$.

to the inner and outer cylinder surfaces corresponds to where the flow cooled by the outer cylinder impinges on the inner cylinder and the flow heated by the inner cylinder impinges on the outer cylinder, respectively. As the Rayleigh number is increased from $Ra = 2000$ to $Ra = 3000$, the isotherms attain a more pronounced S-shaped appearance as a result of the higher rotational strength of the rolls, as seen in figure 4(*b*). Over this Rayleigh number range, the overall Nusselt number increases significantly beyond that of pure conduction, from a value of $Nu_{av} = 1.033$ at $Ra = 2000$ to $Nu_{av} = 1.089$ and 1.143 at $Ra = 2500$ and 3000, respectively.

In studying the stability characteristics of the narrow-gap annulus flow, a procedure was followed in which the Rayleigh number was successively increased in increments starting at a value less than the critical Rayleigh number Ra_c for onset of secondary flows. Each converged solution was used as an initial guess for the next highest Rayleigh number. The value of $Ra_c = 1740$ was determined by plotting results from each converged solution as a function of the Rayleigh number, as shown in figure 5 for the radial velocity at $r = \frac{1}{2}(r_i + r_o)$, $\phi = 0$, $z = \frac{1}{2}L$. The abrupt increase in the upward radial velocity at this location occurring at $Ra_c = 1740$ is indicative of the formation of transverse rolls in the upper portion of the annulus owing to thermal instability. At a Rayleigh number substantially greater than 1740, the process was reversed and carried through until the Rayleigh number was once again below Ra_c. The value of Ra_c thus determined by decreasing the Rayleigh number was found to be the same as that obtained by increasing the Rayleigh number, within the tolerance of the Rayleigh number increment of 10 that was employed. A smaller increment could be used to determine whether or not hysteresis effects are present. However, the computational cost is prohibitive since the numerical solution converges much more slowly as Ra_c is approached owing to the more gradual formation of the secondary flow.

To provide additional insight into the three-dimensional flow structure, fluid particle path plots are presented in figure 6 for $R = 1.1$, $A = 7$ and $Ra = 2500$. In these plots, a particle is introduced into each of the six transverse rolls at positions near the top of the annulus (locations A_1–A_6), and also into four of the transverse rolls at positions closer to the main flow (locations B_1–B_4). The ensuing pathlines show the primary flow features present in the narrow-gap annulus including the interactions between the convective rolls and the main flow. In figures 6(*a*) and 6(*b*), all ten pathlines are

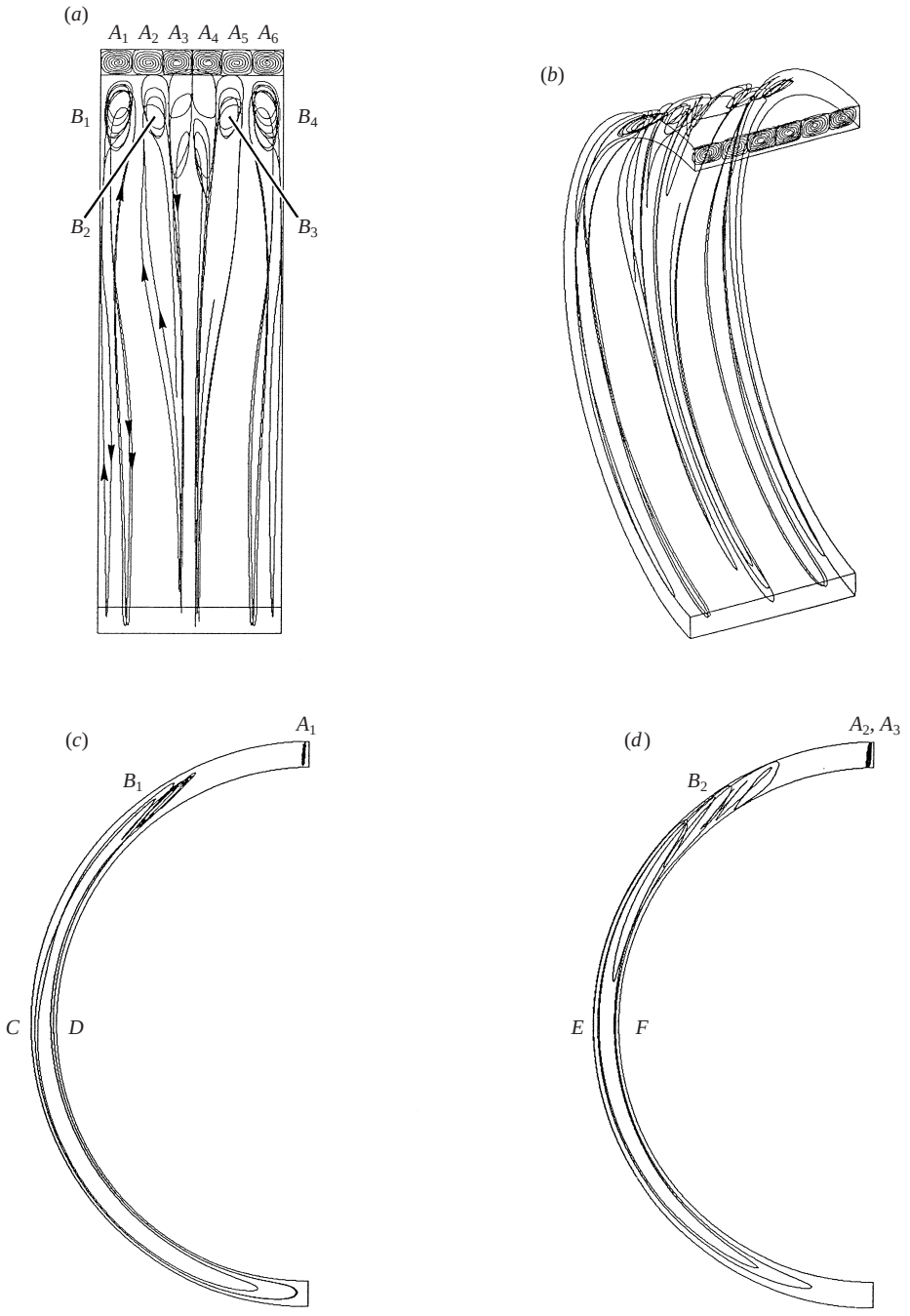

FIGURE 6. Fluid particle paths for the first type of transverse roll pattern for $R = 1.1$, $A = 7$, $Ra = 2500$, $Pr = 0.7$: (*a*) side view; (*b*) perspective view; (*c*) end view of end roll region; (*d*) end view of inner roll pair region.

shown whereas in figures 6(*c*) and 6(*d*), views of the end roll region pathlines and the inner roll pair pathlines, respectively, are shown.

As seen in figures 6(*a*) and 6(*c*), a particle introduced into the centre of an end roll near the top of the annulus (locations A_1 and A_6) traces a series of increasingly larger patterns that reflect the cross-sectional shape of the roll, with only slight movement in the angular direction. Another particle injected into an end roll at a position closer to the main flow (locations B_1 and B_4) exhibits very different behaviour. This particle performs several loops within the roll before becoming entrained in the primary flow, and then follows a crescent-shaped route downward along the outer cylinder (C) to the bottom of the annulus and back up along the inner cylinder (D) to the end roll. At this point it loops over the end roll and then follows another full crescent-shaped route that is closer to the end wall before re-entering the end roll near its release point, thereby closing a three-dimensional circuit. These results indicate that the fluid in the upper portion of the end roll does not interact appreciably with the main flow, whereas that in the lower portion of the roll is part of a three-dimensional circulation involving the end roll and the primary flow. This circulation takes place within the axial boundaries of the end roll.

Particles introduced into the centre of each inner roll near the top of the annulus (locations A_2–A_5) behave similarly to those injected into the upper portion of the end rolls (locations A_1 and A_6), tracing increasingly larger patterns with very little movement in the angular direction, as seen in figures 6(*a*) and 6(*d*). A particle inserted into an inner roll that is adjacent to an end roll at a position closer to the main flow (locations B_2 and B_3) proceeds differently, first moving spirally upward in the annulus and then transferring from this roll to the adjacent inner roll that is next to the mid-axial plane. The particle then traces several loops as it proceeds downward in the annulus and becomes entrained in the primary flow, whereupon it follows a crescent-shaped route to the bottom of the annulus along the outer cylinder (E) and then back up along the inner cylinder (F). The particle returns to the transverse roll where it was introduced, and then traces additional crescent-shaped circuits within the axial boundaries of the inner roll pair. These particle path results show that fluid in the uppermost portion of the inner rolls does not interact appreciably with the main flow, and that three-dimensional circulation patterns involving adjacent pairs of inner rolls and the primary flow are present in the annulus. Since there are two pairs of adjacent inner rolls for the case of $R = 1.1$, $A = 7$ and $Ra = 2500$ considered here, there are two such circulation patterns within the annulus.

The inner and outer cylinder local Nusselt number distributions are plotted in figures 7(*a*) and 7(*b*), respectively, for $R = 1.1$, $A = 7$ and $Ra = 2500$. In the lower third of the annulus (between $\phi = \frac{2}{3}\pi$ and $\phi = \pi$) the inner cylinder Nusselt number shows little variation in the axial direction, and within this region it is highest at the bottom ($\phi = \pi$) where the inner cylinder thermal boundary layer is thinnest. As the fluid rises along the hot inner cylinder the boundary-layer thickness increases and Nusselt number decreases. In the middle third of the annulus (between $\phi = \frac{1}{3}\pi$ and $\phi = \frac{2}{3}\pi$), the inner cylinder Nusselt number begins to vary noticeably in the axial direction as a result of the influence of the transverse rolls on the primary flow. In the upper third (between $\phi = 0$ and $\phi = \frac{1}{3}\pi$), there is much greater variation in the axial direction owing to the direct influence of the transverse rolls. At $\phi = 0$, there are two large peaks in the inner cylinder Nusselt number corresponding to where fluid in the inner roll pairs is first cooled by the outer cylinder and then impinges on the inner cylinder (Nu_{iMAX} in figures 4(*a*) and 4(*b*)). Owing to the greater strength of the inner rolls, these are larger than the local peaks at $z = 0$ and $z = L$ associated with the

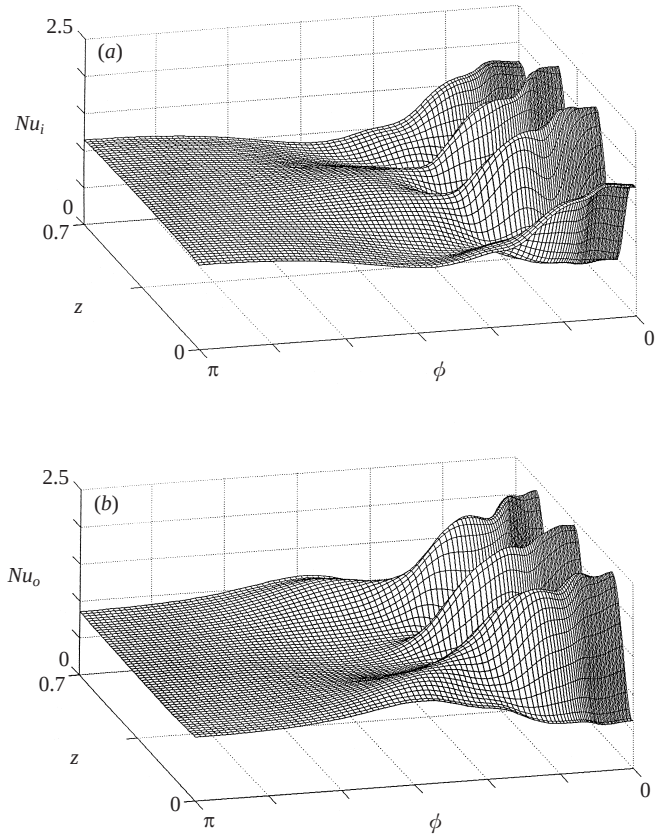

FIGURE 7. Local Nusselt number distributions for the first type of transverse roll pattern for $R = 1.1$, $A = 7$, $Ra = 2500$, $Pr = 0.7$: (*a*) inner cylinder; (*b*) outer cylinder.

end rolls. Between the peaks there are three local minima at $\phi = 0$ corresponding to locations of upward flow away from the inner cylinder, although the perspective in figure 7(*a*) does not clearly show all three minima. The inner cylinder Nusselt number at $\phi = 0$ varies by a factor of 4.88 over the length of the annulus. It is seen that the four peaks associated with the transverse rolls drop-off significantly with increased angular position between approximately $\phi = \frac{1}{12}\pi$ and $\phi = \frac{1}{3}\pi$ as the rolls dissipate. The rate of drop-off temporarily decreases at approximately $\phi = \frac{1}{6}\pi$, which corresponds to where the flow rising along the inner cylinder from the lower portion of the annulus becomes entrained in the transverse rolls.

As shown in figure 7(*b*), in the lower portion of the annulus, the outer cylinder Nusselt number is essentially independent of axial position, becomes smaller with increased angular position, and is a minimum at $\phi = \pi$. The trend of decreasing magnitude with increased angular position occurs since the outer cylinder thermal boundary layer increases in thickness as the flow proceeds downward. In the middle portion of the annulus, the outer cylinder Nusselt number begins to vary significantly in the axial direction as a result of the influence of the transverse rolls on the primary flow, as was the case for the inner cylinder Nusselt number. In the upper part of the annulus, the outer cylinder Nusselt number shows a dramatic variation in the axial direction resulting from the inner roll pairs. There are three local maxima occurring

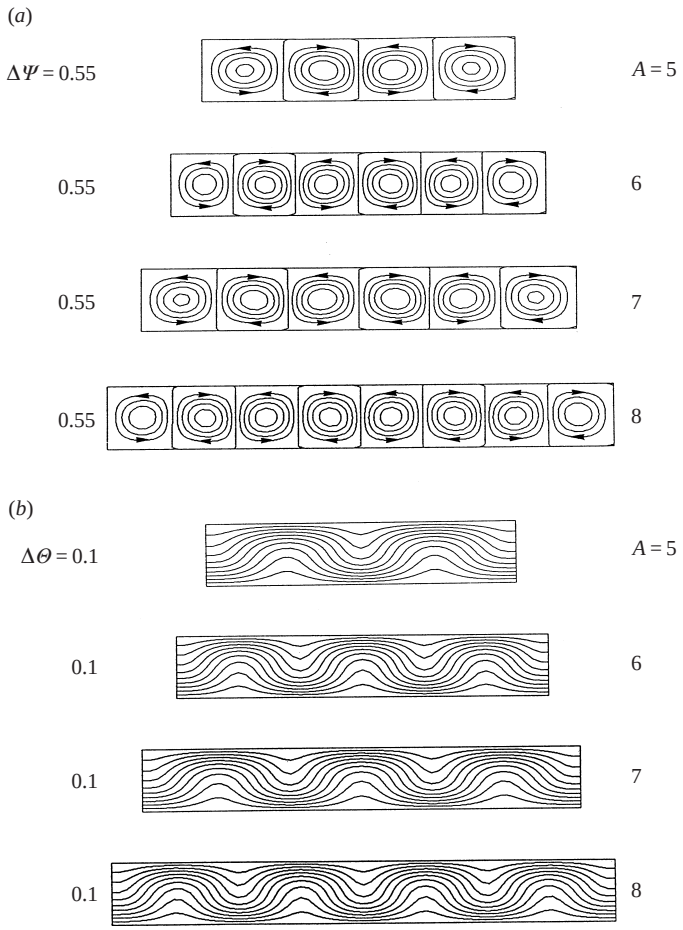

FIGURE 8. Effect of A on convection at the upper vertical angular plane for the first type of transverse roll pattern for $R = 1.1$, $Ra = 2500$, $Pr = 0.7$: (a) streamlines; (b) isotherms.

at $\phi = 0$ which are associated with the flow in the rolls moving upward from the hot inner cylinder and meeting the cool outer cylinder (Nu_{oMAX} in figures 4(a) and 4(b)). There are also four local minima at $\phi = 0$ corresponding to the locations of downward movement of fluid away from the outer cylinder, even though these are not all clearly shown in the figure 7(b) view. The outer cylinder Nusselt number at $\phi = 0$ varies by a factor of 4.20 over the length of the annulus. The locations where the flow rising along the inner cylinder becomes entrained in the transverse rolls coincide with three local maxima present at approximately $\phi = \frac{1}{6}\pi$.

The streamlines and isotherms in the upper vertical angular planes of annuli with gap aspect ratios of $A = 5$, 6, 7 and 8 are presented in figure 8 for $Ra = 2500$. From these results, it is seen that as the aspect ratio is successively increased from $A = 5$ to $A = 8$ in increments of $\Delta A = 1$, either the existing rolls expand or additional inner rolls form, always one counter-rotating roll pair at a time. The total number of rolls and sizes of the inner rolls are given in table 1 as a function of A. It can be seen that the size of the inner rolls varies somewhat to accommodate an integral number of roll pairs between the end rolls. The roll sizes given in table 1 are within -3% to $+18\%$ of the theoretical size of $l' = 0.101$ for an infinite length annulus calculated using

Aspect ratio A	Number of rolls	Inner role size (dimensionless)
5	4	0.119
6	6	0.099
7	6	0.114
8	8	0.098

TABLE 1. Number and size of transverse rolls in the annulus for $R = 1.1$ and $Ra = 2500$.

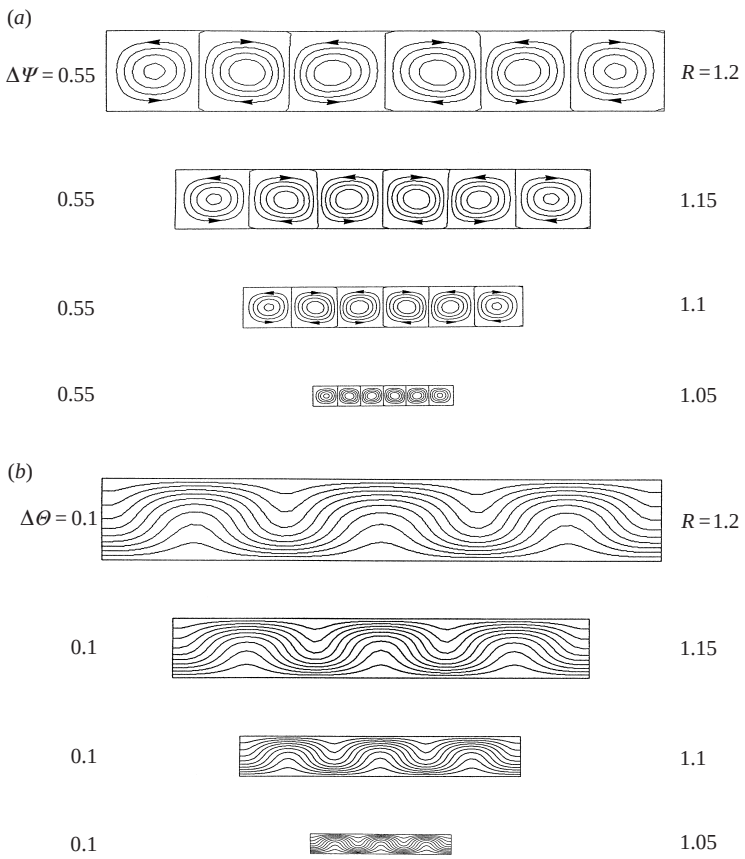

FIGURE 9. Effect of R on convection at the upper vertical angular plane for the first type of transverse roll pattern for $A = 7$, $Ra = 2500$, $Pr = 0.7$: (a) streamlines; (b) isotherms.

$l' = m\pi(r_o - r_i)/S_{cL}$, with $m = 1$ being the number of cells and $S_{cL} = 3.12$ being the critical wavenumber obtained from the linear stability analysis of Dyko *et al.* (1999).

Simulations were also performed for $R = 1.05$, 1.15 and 1.2 with $A = 7$ and $Ra = 2500$ to investigate the effect of radius ratio R on the transverse rolls. The streamlines and isotherms in the upper vertical angular plane associated with each of these cases and the baseline case of $R = 1.1$, $A = 7$ and $Ra = 2500$ are plotted in figures 9(a) and 9(b), respectively. It can be seen that for all of the cases, a total of six transverse rolls form in the upper portion of the annulus. The maximum value of the stream function at the upper vertical angular plane associated with the inner rolls

varies by less than 2% over the range $1.05 \leqslant R \leqslant 1.2$. Consequently, the appearance of the isotherms is essentially unchanged over this range. These results indicate that, for $A = 7$ and $Ra = 2500$, within the range of R studied, the radius ratio does not affect the number of transverse rolls nor does it significantly affect the dimensionless strength of the transverse rolls.

The orientation and directions of rotation of the counter-rotating supercritical rolls presented up to this point are determined by end rolls that are present at subcritical Rayleigh numbers and become stronger as the Rayleigh number is increased above Ra_c, which is approximately 1740 for $R = 1.1$. These end rolls, which are driven by the main flow and form because of the viscous shear imposed by the endwalls, are oriented in the transverse direction and rotate clockwise and counterclockwise on the right- and left-hand sides of the annulus, respectively. The shear force they exert on the fluid in the inner region induces the formation of supercritical transverse rolls and determines the directions of rotation of these rolls.

In the absence of perturbations in the flow and temperature fields, these end rolls develop prior to formation of the supercritical rolls when starting from a quiescent and isothermal initial state and increasing the Rayleigh number to a value above Ra_c, resulting in the same transverse supercritical rolls as described so far. In nature and experiments, however, small disturbances that trigger the inception of instabilities cannot be eliminated and it is possible for the supercritical rolls to arise prior to the development of these end rolls. In such a situation, the orientation and directions of roll rotation are no longer predetermined and different supercritical roll patterns can develop. In a numerical simulation where round-off errors are negligibly small, disturbances must be deliberately introduced to simulate this process. This is accomplished in the present study through the use of appropriate initial conditions.

In order to prompt formation of supercritical transverse rolls prior to development of the aforementioned end rolls, the equation (29) perturbed conductive temperature field that is periodic in the z-direction is introduced at $t = 0$. As mentioned previously, equation (29) physically represents the reversal of thermal gradients associated with inception of thermal instabilities in the annulus. Simulations were conducted in which η was varied over the full range of $0 \leqslant \eta \leqslant 2\pi$, with C_B based on the solution obtained by successively increasing the Rayleigh number to supercritical values. It was found that one of two types of steady transverse roll patterns develops depending on the value of η. The first type is identical to that obtained by successively increasing the Rayleigh number from subcritical to supercritical values as plotted in figure 4, with end rolls that rotate clockwise and counterclockwise on the right- and left-hand sides of the annulus, respectively. The second type exhibits the same number of transverse rolls, but with reversed directions of roll rotation. Thus, for the second type, the end rolls rotate counterclockwise and clockwise on the right- and left-hand sides of the annulus, respectively. It is noted that the existence of rolls with reversed directions of rotation can also be found in Rayleigh–Bénard convection between horizontal planes, in which two branches of solutions corresponding to clockwise and counterclockwise roll rotation bifurcate from the hydrostatic solution at $Ra = Ra_c$.

The streamlines and isotherms in the upper vertical angular plane associated with the second type of transverse roll pattern are plotted in figures 10(a) and 10(b), respectively, for $R = 1.1$ and $A = 7$ at Rayleigh numbers of $Ra = 2000$, 2500 and 3000. As seen by comparing figure 10(a) with figure 4(a), at each of these supercritical Rayleigh numbers, the number of transverse rolls is the same as for the first type of transverse roll pattern, but the direction of rotation of each roll is reversed. Note that at the subcritical Rayleigh number of $Ra = 1500$ ($Ra_c = 1740$ for $R = 1.1$),

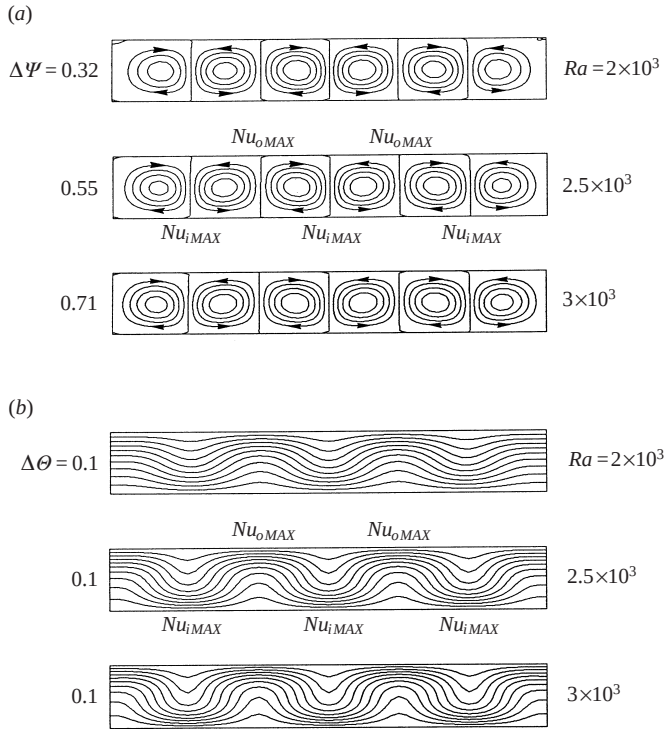

FIGURE 10. Effect of Ra on convection at the upper vertical angular plane for the second type of transverse roll pattern for $R = 1.1$, $A = 7$, $Pr = 0.7$: (*a*) streamlines; (*b*) isotherms.

the same final solution as that shown in figures 4(*a*) and 4(*b*) is obtained using the equation (29) initial condition. Owing to the reversed directions of rotation of the transverse rolls, the alternating elevation and depression of isotherms along the length of the annulus for the second type of transverse roll pattern is opposite to that of the first type, as seen by comparing figure 10(*b*) with figure 4(*b*). The axial locations of impingement regions on the inner cylinder, as indicated by the closer spacing of isotherms next to the inner cylinder seen in figure 10(*b*), correspond to those on the outer cylinder for the first type of transverse roll pattern seen in figure 4(*b*). Likewise, the axial positions of impingement regions on the outer cylinder correspond to those on the inner cylinder for the first type of pattern. As the Rayleigh number is increased from $Ra = 2000$ the overall Nusselt number increases from a value of $Nu_{av} = 1.028$ to $Nu_{av} = 1.085$ and 1.142 at $Ra = 2500$ and 3000, respectively. Therefore, over this Rayleigh number range the overall annulus heat transfer is essentially unchanged compared to the first type of transverse roll pattern.

The bifurcation point for the second type of transverse roll pattern was found to be approximately $Ra = 1950$ (within a Rayleigh number increment of 50) for $R = 1.1$, as indicated in figure 5. For Rayleigh numbers between $Ra_c = 1740$ and approximately $Ra = 1950$, the second type of transverse roll pattern initially forms using the equation (29) initial condition, but as time progresses the flow transitions to the first type of transverse roll pattern. This transition occurs owing to a gradual dissipation of the second type of end roll (counterclockwise and clockwise rotation on the right- and left-hand sides of the annulus, respectively) and resulting formation

of the first type of end roll (clockwise and counterclockwise rotation on the right- and left-hand sides of the annulus, respectively).

The plots shown in figure 5 for the first and second types of transverse roll patterns and the subcritical flow provide evidence of an imperfect bifurcation for transverse rolls in a narrow-gap annulus. The pitchfork bifurcation associated with Rayleigh–Bénard convection between horizontal planes degenerates into this imperfect bifurcation owing to the curvature of the inner and outer cylinders, the presence of the end walls, and the interaction of the transverse rolls with the primary flow. The rolls associated with the first type of transverse roll pattern interact with the primary flow somewhat differently to those associated with the second type (as described next), which contributes to the asymmetry of the two branches of supercritical solutions seen in figure 5. It is noted that the figure 5 bifurcation diagram for transverse rolls is similar in appearance to the bifurcation diagrams for two-dimensional cellular flow in a narrow-gap annulus presented by Cadiou *et al.* (1998), even though the flow patterns are very different.

Fluid particle path plots for the second type of transverse roll pattern are presented in figure 11 for $R = 1.1$, $A = 7$ and $Ra = 2500$. In the same manner as previously shown in figure 6 for the first type of transverse roll pattern, a particle is introduced into each of the six transverse rolls at positions near the top of the annulus (locations A_1–A_6), and also into four of the transverse rolls at positions closer to the main flow (locations B_1–B_4). In figure 11, however, the locations B_2 and B_3 are now within the two innermost rolls, rather than the inner rolls that are adjacent to the end rolls.

As seen in figures 11(*a*) and 11(*b*), particles introduced into the centre of each transverse roll near the top of the annulus (locations A_1–A_6) behave similarly to the corresponding particles shown in figure 6 for the first type of transverse roll pattern. Each of these particles traces increasingly larger patterns with very little movement in the angular direction. Therefore, the fluid in the upper portions of the transverse rolls does not interact appreciably with the main flow, as was the case for the first type of transverse roll pattern (figure 6).

A particle injected into an end roll at a position closer to the main flow (locations B_1 and B_4) exhibits behaviour different from the corresponding particle for the first type of transverse roll pattern. As shown in figures 11(*a*) and 11(*c*), for the second type of transverse roll pattern this particle spirals downward within the end roll and then becomes entrained in the primary flow. It subsequently follows a crescent-shaped route downward along the outer cylinder (C) to the bottom of the annulus and back up along the inner cylinder (D). After this, it enters the inner roll that is adjacent to the end roll, spirals upward in the annulus, and transfers from this inner roll to the end roll near its release point, thereby closing a three-dimensional circuit. It is thus shown that the three-dimensional circulation at the end of the annulus now involves the end roll, the adjacent inner roll, and the primary flow instead of just the end roll and the primary flow as in the first type of transverse roll pattern.

In figures 11(*a*) and 11(*d*), it can be seen that a particle inserted into one of the two innermost rolls at a position close to the main flow (locations B_2 and B_3) traces several loops before becoming entrained in the primary flow, and then follows a crescent-shaped route towards the bottom of the annulus along the outer cylinder (E) and back up along the inner cylinder (F), whereupon it re-enters the innermost roll. The particle subsequently traces several crescent-shaped routes that show greater axial movement toward the end wall prior to returning to the innermost roll. These particle path results for the second type of transverse roll pattern indicate that three-dimensional circulation patterns involving a single innermost roll and the primary

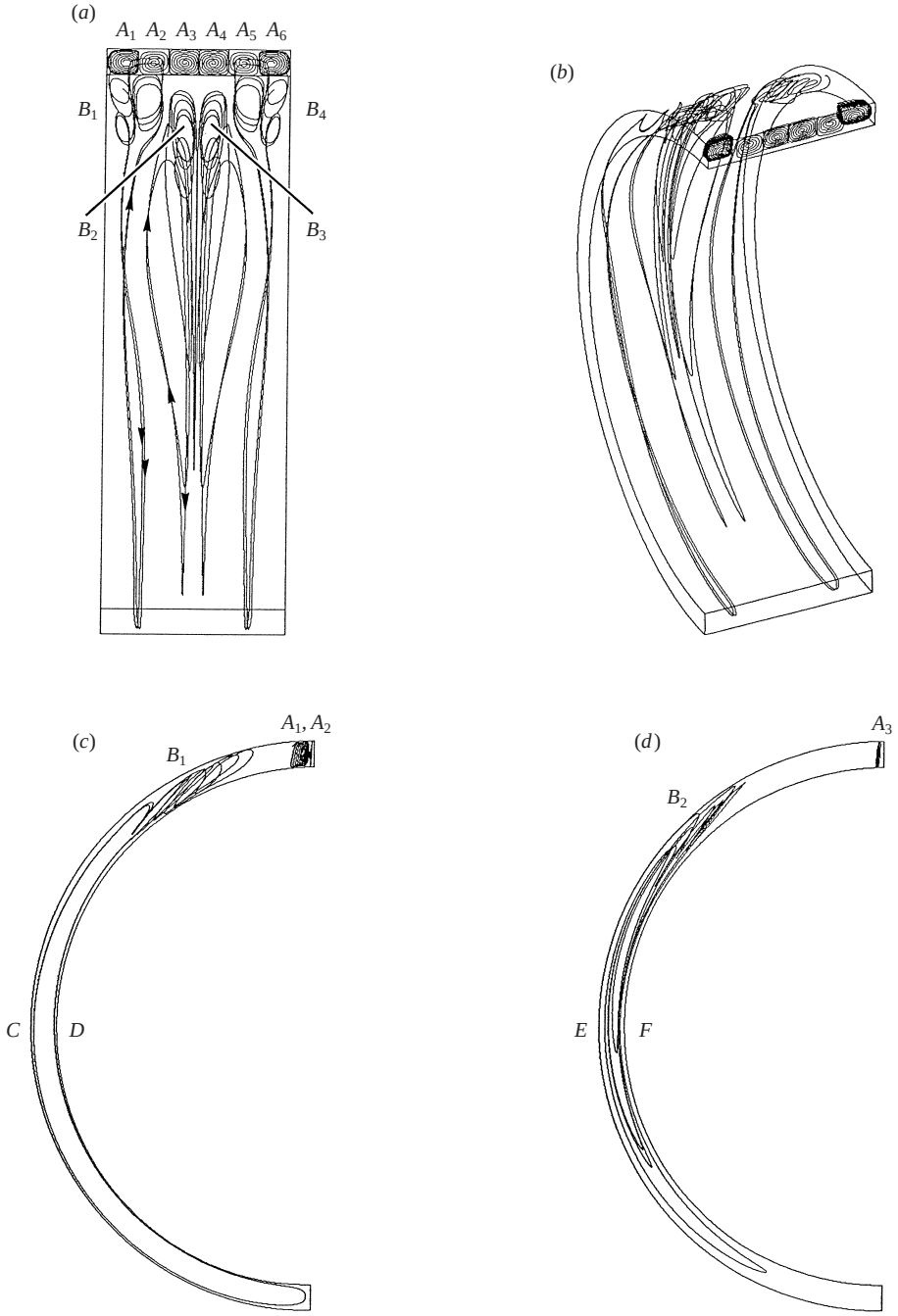

FIGURE 11. Fluid particle paths for the second type of transverse roll pattern for $R = 1.1$, $A = 7$, $Ra = 2500$, $Pr = 0.7$: (*a*) side view; (*b*) perspective view; (*c*) end view of end roll and adjacent inner roll region; (*d*) end view of innermost roll region.

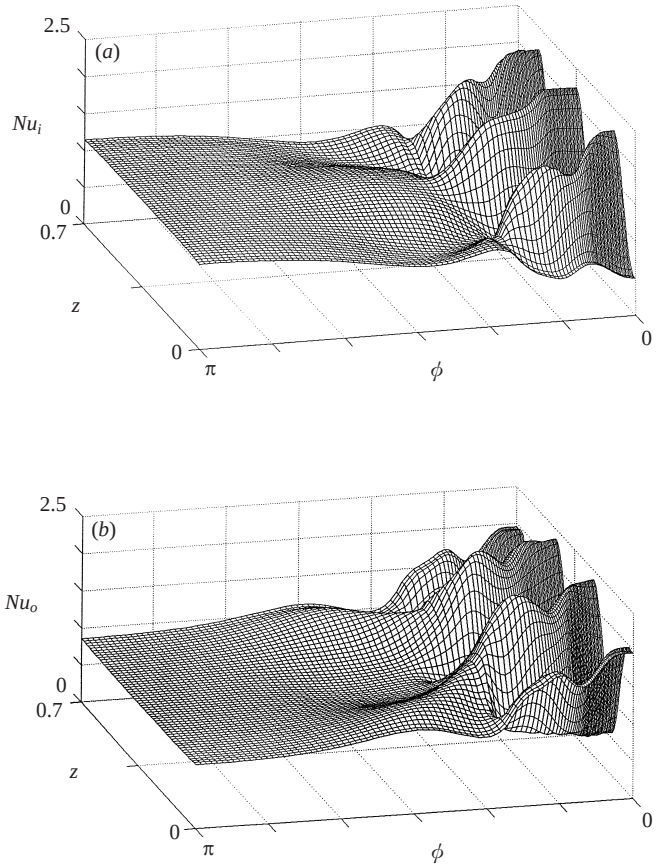

FIGURE 12. Local Nusselt number distributions for the second type of transverse roll pattern for $R = 1.1$, $A = 7$, $Ra = 2500$, $Pr = 0.7$: (*a*) inner cylinder; (*b*) outer cylinder.

flow are present in the annulus. Since there are two innermost rolls, there are two such circulation patterns within the annulus. These patterns are therefore different from those associated with the first type of transverse roll pattern, in which the innermost rolls are each paired with an adjacent inner roll in a circulation pattern.

The inner and outer cylinder local Nusselt number distributions for the second type of transverse roll pattern are plotted in figures 12(*a*) and 12(*b*), respectively, for $R = 1.1$, $A = 7$ and $Ra = 2500$. The inner cylinder Nusselt number distribution in the lower two-thirds of the annulus is seen to be nearly the same as that shown in figure 7(*a*) for the first type of transverse roll pattern. In the upper portion of the annulus, however, there are significant changes resulting from the reversed directions of rotation of the rolls. At $\phi = 0$, there are now three local maxima (rather than two large peaks and two smaller peaks) corresponding to where fluid entrained in the rolls is first cooled by the outer cylinder and then impinges on the inner cylinder (Nu_{iMAX} in figures 10*a* and 10*b*). There are also four local minima at $\phi = 0$ (rather than three), although all of these are not clearly seen in this view. The inner cylinder Nusselt number at $\phi = 0$ varies by a factor of 4.69 over the length of the annulus. As is the case for the first type of transverse roll pattern, the peaks associated with the transverse rolls drop-off significantly with increased angular position between

approximately $\phi = \frac{1}{12}\pi$ and $\phi = \frac{1}{3}\pi$ as the rolls dissipate. This drop-off is temporarily interrupted at approximately $\phi = \frac{1}{6}\pi$, which corresponds to where the flow rising along the inner cylinder from the lower portion of the annulus becomes entrained in the transverse rolls.

It is seen by comparing figure 12(*b*) with figure 7(*b*) that the outer cylinder Nusselt number distribution in the lower two-thirds of the annulus for the second type of transverse roll pattern is close to that for the first type of transverse roll pattern. In the upper part of the annulus, however, the outer cylinder Nusselt number distribution is significantly changed owing to the reversed roll rotation. There are now two large peaks at $\phi = 0$ that are associated with the flow in the inner roll pairs being heated by the inner cylinder and then impinging on the outer cylinder (Nu_{0MAX} in figures 10*a* and 10*b*), and also two smaller peaks at $z = 0$ and $z = L$ associated with the end rolls (rather than three maxima). There are also three local minima at $\phi = 0$ (rather than four) corresponding to the locations of downward movement of fluid away from the outer cylinder. These minima can be clearly seen from a different perspective. The outer cylinder Nusselt number at $\phi = 0$ varies by a factor of 4.08 over the length of the annulus. The locations where the flow rising along the inner cylinder becomes entrained in the transverse rolls coincide with the four local maxima present at approximately $\phi = \frac{1}{6}\pi$.

In addition to the cases analysed for $R = 1.1$ with $A = 7$, simulations were performed for $A = 5$, 6 and 8 with $R = 1.1$ and $Ra = 2500$, and for $R = 1.05$, 1.15 and 1.2 with $A = 7$ and $Ra = 2500$ to investigate the effects of annulus aspect ratio A and radius ratio R, respectively, on the second type of transverse roll pattern. From these simulations, it was found that the overall effects of varying A and R on the second type of roll pattern are the same as those previously discussed for the first type of roll pattern.

3.2. *Combinations of longitudinal and transverse rolls*

Three-dimensional natural convective flow comprised of longitudinal rolls in the top portion of the annulus, transverse rolls adjacent to the longitudinal rolls, and the primary recirculating flow in the middle and lower regions is investigated in this section. Simulations were performed for an air-filled annulus of radius ratio $R = 1.1$ and gap aspect ratio $A = 7$, which are the same baseline parameters used in the investigation of supercritical flows exhibiting only transverse rolls in the upper annulus discussed in § 3.1. Results for Rayleigh numbers ranging from $Ra = 2000$ to $Ra = 3000$ are presented to illustrate the evolution of supercritical flow structures with increasing Rayleigh number. Results are also presented for $R = 1.05$ and 1.15 to demonstrate the influence of radius ratio on the flow fields and temperature distributions.

The equation (30) perturbed conductive temperature field, which is periodic in the angular direction, was introduced at $t = 0$ to induce the formation of supercritical longitudinal rolls prior to development of transverse end rolls. As noted earlier, equation (30) simulates the reversal of thermal gradients associated with the onset of thermal instabilities in the annulus. Numerical simulations were performed in which the phase shift η was successively varied over the full range of $0 \leqslant \eta \leqslant 2\pi$, with C_B based on the theoretical wavenumber obtained using linear stability theory. It was found that at sufficiently high Rayleigh numbers, one of two types of steady longitudinal roll patterns that are symmetric with respect to the vertical angular plane develops depending on the value of η. The first type has a downward radial velocity at the upper vertical angular plane, and the second type an upward radial

velocity. Hence, the directions of rotation of the rolls for one type of longitudinal roll pattern are opposite to those of the other type. Note that longitudinal rolls that are asymmetric with respect to the vertical angular plane form initially when η is set to a value other than zero or an integer multiple of π. However, it was found that these rolls become symmetric after a sufficient period of time passes, resulting in one of the two types of final roll patterns. For the purposes of illustrating the fundamental behaviour of longitudinal rolls that initially set up in the annulus (and persist undiminished until the development of transverse rolls) and comparing these initial longitudinal rolls to the steady cells obtained in previous two-dimensional numerical studies (see figure 3), the results presented herein for early times in the transient development of the flow field correspond to η of zero or an integer multiple of π.

In the discussions that follow, a longitudinal roll is characterized as fully separated from the main flow if, when viewed in the mid-axial plane, it is bounded on each side by a streamline that extends radially between the inner and outer cylinders. These fully separated rolls are designated by Arabic numerals in the figures. Rolls that are either bounded on only one side by a radial streamline or are not bounded by any radial streamlines are considered to be partially separated from the main flow, and are designated in the figures by Roman numerals.

Streamlines and isotherms in the mid-axial plane associated with the first type of longitudinal roll pattern (downward radial velocity at the upper vertical angular plane) are plotted on the left-hand side of figure 13(*a*) for $Ra = 2000$ at a time early in the transient response of the fluid of $t = 0.005$. It is seen that at $t = 0.005$, a single fully separated rotational cell (1) has formed on the left-hand side of the upper vertical angular plane. There is a corresponding counter-rotating cell on the right-hand side of this plane, for a total of two fully separated cells at the top of the annulus. Each cell is actually a cross-section of a fully separated longitudinal roll (1) extending along the length of the annulus that is set apart from the main crescent-shaped flow by two partially separated rolls (II, III), which are also shown on the left-hand side of figure 13(*a*). The S-shaped appearance of the isotherms in the upper portion of the annulus reflects the alternating directions of rotation of the fully and partially separated rolls. The flow remains steady and two-dimensional at the mid-axial region until approximately $t = 0.01$, at which time transverse rolls begin to form there. It is observed on the right-hand side of figure 13(*a*) that when steady state conditions are achieved at $t \geqslant 0.15$, the longitudinal rolls have completely dissipated. By this time, transverse rolls have replaced the longitudinal rolls and the flow structure is identical to that shown in figure 4 for $Ra = 2000$. These results show that at $Ra = 2000$, the strength of the longitudinal rolls is insufficient to prevent their eventual displacement by transverse rolls.

At a Rayleigh number of $Ra = 2500$, the partially separated rolls on each side of the annulus gain strength and become two additional fully separated longitudinal rolls (2, 3) as seen on the left-hand side of figure 13(*b*), for a total of six fully separated counter-rotating rolls in the upper region at $t = 0.005$. Also, there is evidence of two additional rolls (IV, V) beginning to separate from the main flow as indicated by the narrowing of streamlines and distortion of isotherms near the tip of the main crescent-shaped flow. The longitudinal rolls present for $Ra = 2500$ at $t = 0.005$ are stronger than the corresponding rolls present for $Ra = 2000$ at this same time, as indicated by the plotted streamlines, increased value of $\Delta\Psi$, and more pronounced S-shaped appearance of isotherms on the left-hand side of figure 13(*b*) compared to the left-hand side of figure 13(*a*). The strength of the longitudinal rolls at $Ra = 2500$

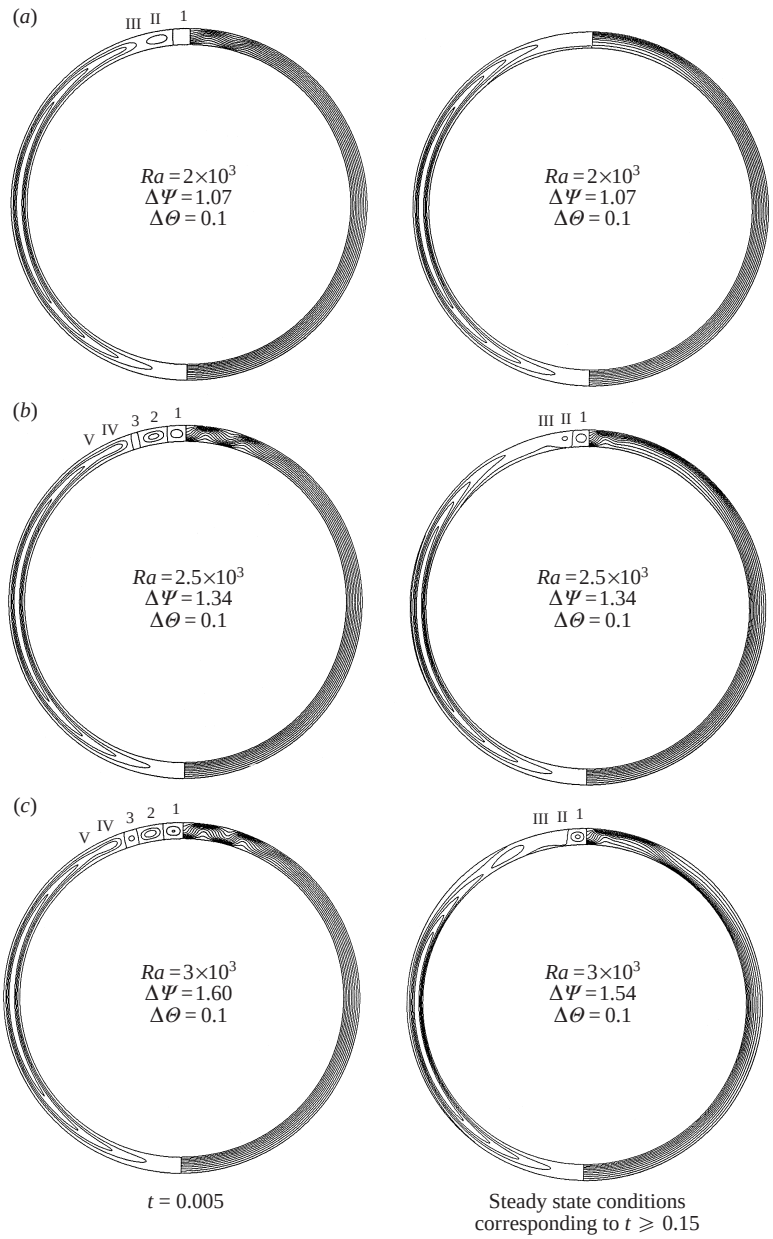

FIGURE 13. Effect of Ra on convection at the mid-axial plane for the first type of longitudinal roll pattern for $R = 1.1$, $A = 7$, $Pr = 0.7$, with streamlines on the left-hand sides and isotherms on the right-hand sides at $t = 0.005$ and steady state: (*a*) $Ra = 2000$; (*b*) $Ra = 2500$; (*c*) $Ra = 3000$.

is now sufficient that the transverse rolls no longer displace all of the longitudinal rolls at steady state. Instead, as shown on the right-hand side of figure 13(*b*) for $t \geqslant 0.15$, on each side of the upper vertical angular plane there exists a single fully separated longitudinal roll (1) accompanied by two weak counter-rotating regions (II, III). Although not obvious in this figure showing results at the mid-axial plane, transverse rolls are in place between the longitudinal rolls (accompanied by weak

counter-rotating regions) and the main flow. There are a total of two fully separated longitudinal rolls and four weak counter-rotating regions at the top of the annulus that separate six transverse rolls on one side of the annulus from six corresponding transverse rolls on the other side. It is thus shown that at a sufficiently high Rayleigh number, another type of final supercritical roll pattern exists that is comprised of both longitudinal and transverse rolls in the upper part of the annulus.

At a Rayleigh number of $Ra = 3000$, three fully separated longitudinal rolls (1, 2, 3) once again form on each side of the annulus (six fully separated rolls total in the upper region) at $t = 0.005$ as seen on the left-hand side of figure 13(c). The strength and angular extent of these rolls has increased, as seen by comparing the streamlines and isotherms plotted on the left-hand side of figure 13(c) to the corresponding ones in figure 13(b) for $Ra = 2500$. By comparing the streamlines and isotherms at $t = 0.005$ in figure 13(c) for $Ra = 3000$ to the corresponding ones in figures 13(a) and 13(b) for $Ra = 2000$ and $Ra = 2500$, respectively, the trends of an increasing number of fully separated longitudinal rolls and greater angular extent of these rolls with higher Rayleigh number are clearly evident. These trends are consistent with the increase in angular extent of cellular flow observed in the experimental studies of natural convection of air in a long narrow-gap horizontal annulus conducted by Liu *et al.* (1961). As shown on the right-hand side of figure 13(c) for $t \geqslant 0.15$, the final flow structure after development of the adjoining transverse rolls at $Ra = 3000$ is similar to that present at $Ra = 2500$. Once again, a total of two fully separated longitudinal rolls and four weak counter-rotating regions at the top of the annulus separate six transverse rolls on each side of the annulus. The strength of the rolls at $Ra = 3000$ is greater than at $Ra = 2500$. The steady state overall Nusselt numbers for the first type of longitudinal roll pattern shown on the right-hand sides of figures 13(b) and 13(c) are $Nu_{av} = 1.084$ and 1.136 for $Ra = 2500$ and 3000, respectively. These values are only slightly lower than the corresponding Nusselt numbers for the first and second types of transverse roll patterns discussed in § 3.1, and indicate a substantial increase in heat transfer beyond that of pure conduction.

The pathlines of particles introduced into the annulus at positions close to the main flow (locations B_1–B_4) for the first type of longitudinal roll pattern for $R = 1.1$, $A = 7$, and $Ra = 2500$ are essentially the same as those shown in figure 6 for the first type of transverse roll pattern, and thus are not presented. Particles released into the longitudinal rolls themselves trace a series of increasingly larger patterns that reflect the cross-sectional shape of the rolls, except now these patterns are rotated 90° (compared to the transverse roll patterns) owing to the roll orientation. There is relatively little movement of these particles in the axial direction, and the fluid within the longitudinal rolls does not interact appreciably with the main flow. It is noted that the above description of overall fluid movement in the annulus also applies to the second type of longitudinal roll pattern discussed later, except that the particles released into a given longitudinal roll rotate in the opposite direction owing to the reversed directions of roll rotation.

The inner and outer cylinder Nusselt number distributions for the first type of longitudinal roll pattern are shown in figures 14(a) and 14(b), respectively, for $R = 1.1$, $A = 7$ and $Ra = 2500$. It is seen that below the longitudinal rolls (between approximately $\phi = \frac{1}{12}\pi$ and $\phi = \pi$), the inner and outer cylinder Nusselt number distributions are essentially the same as those shown in figures 7(a) and 7(b) for the first type of transverse roll pattern, except the peaks in inner cylinder Nusselt number associated with the transverse rolls (now located between the longitudinal rolls and the main flow) are slightly greater than before. In figure 14(a), a large perturbation

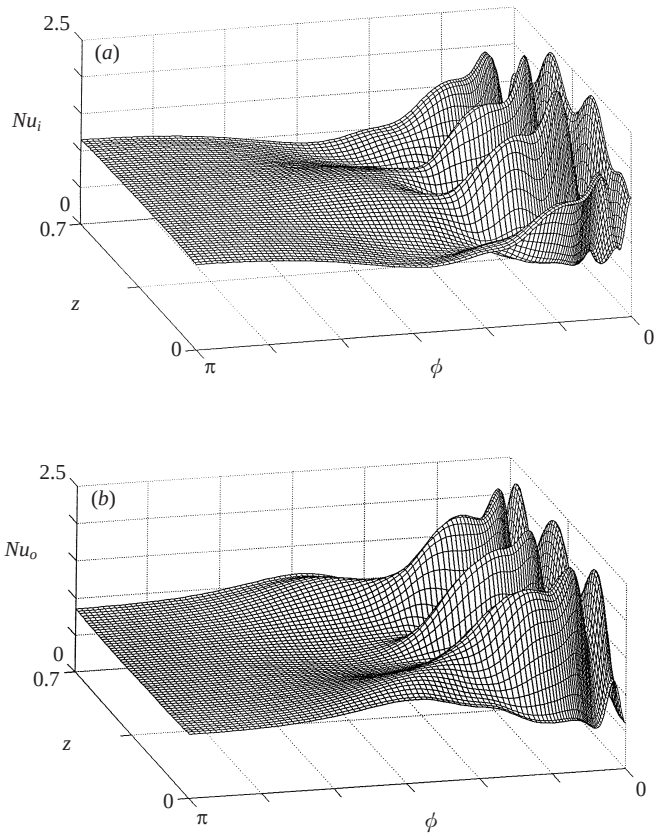

FIGURE 14. Local Nusselt number distributions for the first type of longitudinal roll pattern for $R = 1.1$, $A = 7$, $Ra = 2500$, $Pr = 0.7$: (*a*) inner cylinder; (*b*) outer cylinder.

in the inner cylinder Nusselt number distribution near $\phi = 0$ that extends axially across the entire annulus is seen to occur as a result of the longitudinal roll next to $\phi = 0$. The local peak values of Nusselt number along the length of the annulus at $\phi = 0$ reflect the downward movement of fluid from the cool outer cylinder to the hot inner cylinder owing to this longitudinal roll. The inner cylinder Nusselt number at $\phi = 0$ varies by a factor of 1.51 over the length of the annulus, which is much less than for the transverse roll patterns. In figure 14(*b*), a large perturbation in the outer cylinder Nusselt number distribution near $\phi = 0$ that extends axially across the entire annulus is seen to occur owing to the longitudinal roll. The local minimum values of the Nusselt number along the length of the annulus at $\phi = 0$ reflect the downward movement of fluid away from the outer cylinder. The outer cylinder Nusselt number at $\phi = 0$ varies by a factor of 1.53 over the length of the annulus, which again is much less than for the transverse roll patterns.

The streamlines and isotherms in the upper portion of the mid-axial plane at $Ra = 2500$ are plotted in figures 15(*a*), 15(*b*) and 15(*c*) for annulus radius ratios of $R = 1.15$, 1.1 and 1.05, respectively. As seen on the left-hand sides of these figures, the number of fully separated longitudinal rolls on each side of the vertical angular plane that set up early-on increases from one (1) to three $(1, 2, 3)$ to five $(1, 2, 3, 4, 5)$ as R decreases in increments of $\Delta R = 0.05$ starting from $R = 1.15$. From the right-hand side of figure 15(*a*), it can be seen that at steady state conditions there are no final longitudinal

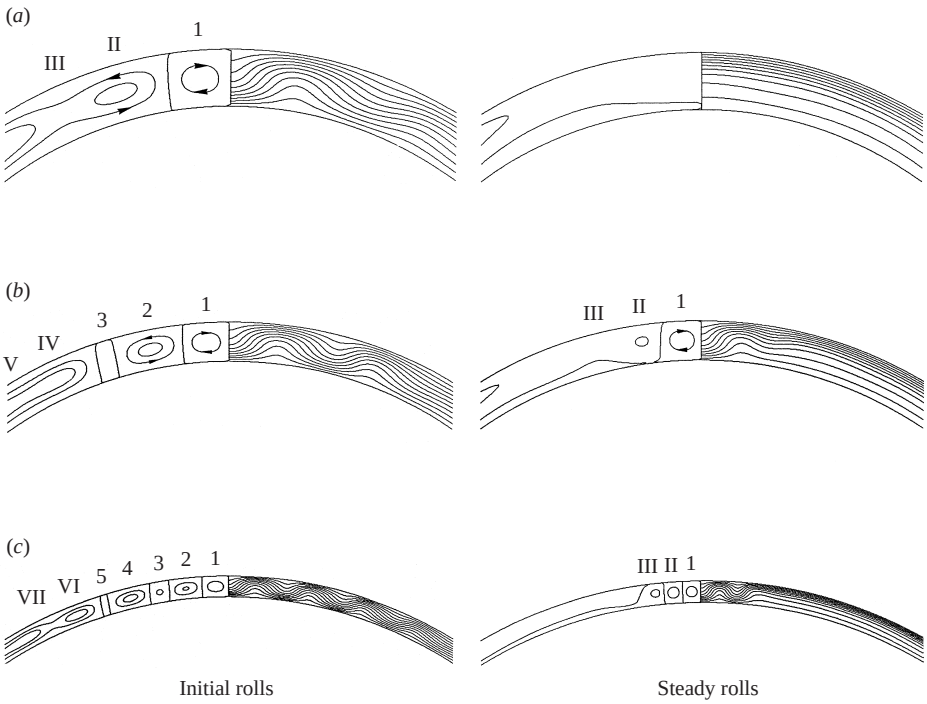

FIGURE 15. Effect of R on convection at the upper portion of the mid-axial plane for the first type of longitudinal roll pattern (downward radial velocity at $\phi = 0$) for $A = 7$, $Ra = 2500$, $Pr = 0.7$, with streamlines on the left-hand sides and isotherms on the right-hand sides for initial rolls and steady rolls: (*a*) $R = 1.15$; (*b*) $R = 1.1$; (*c*) $R = 1.05$.

rolls present for $R = 1.15$. For $R = 1.1$ and $R = 1.05$, one final fully separated longitudinal roll (1) is accompanied by two counter-rotating regions (II, III) on each side of the annulus at steady state as shown on the right-hand sides of figures 15(*b*) and 15(*c*), respectively. The results presented in figures 15(*a*)–15(*c*) indicate that an odd number of longitudinal rolls always sets up on each side of the annulus for the first type of longitudinal roll pattern (downward radial velocity at the upper vertical angular plane). This occurs since, for this type of pattern, the directions of rotation of the uppermost roll and the roll adjacent to the main flow are both opposite that of the main flow, which is possible only for an odd number of counter-rotating rolls. The results also show that the first type of longitudinal roll pattern is sustained at steady state for annulus radius ratios less than a critical value R_1, where $1.1 < R_1 < 1.15$. When $R > R_1$, the transverse rolls supplant the longitudinal rolls at steady state.

The streamlines and isotherms in the upper portion of the mid-axial plane associated with the second type of longitudinal roll pattern (upward radial velocity at the upper vertical angular plane) are plotted in figures 16(*a*), 16(*b*) and 16(*c*) for $R = 1.15$, 1.1 and 1.05, respectively, at $Ra = 2500$. It can be seen from the left-hand sides of these figures that the number of fully separated longitudinal rolls on each side of the annulus that set up early-on increases from two $(1, 2)$ to four $(1, 2, 3, 4)$ as R decreases from $R = 1.15$ to $R = 1.05$. It is also seen from the right-hand sides of figures 16(*a*) and 16(*b*) that at $t \geqslant 0.15$ there are no final longitudinal rolls present for either $R = 1.15$ or $R = 1.1$. For $R = 1.05$, there are two fully separated longitudinal rolls (1, 2) and two counter-rotating regions (III, IV) present on each side of the annulus at steady state,

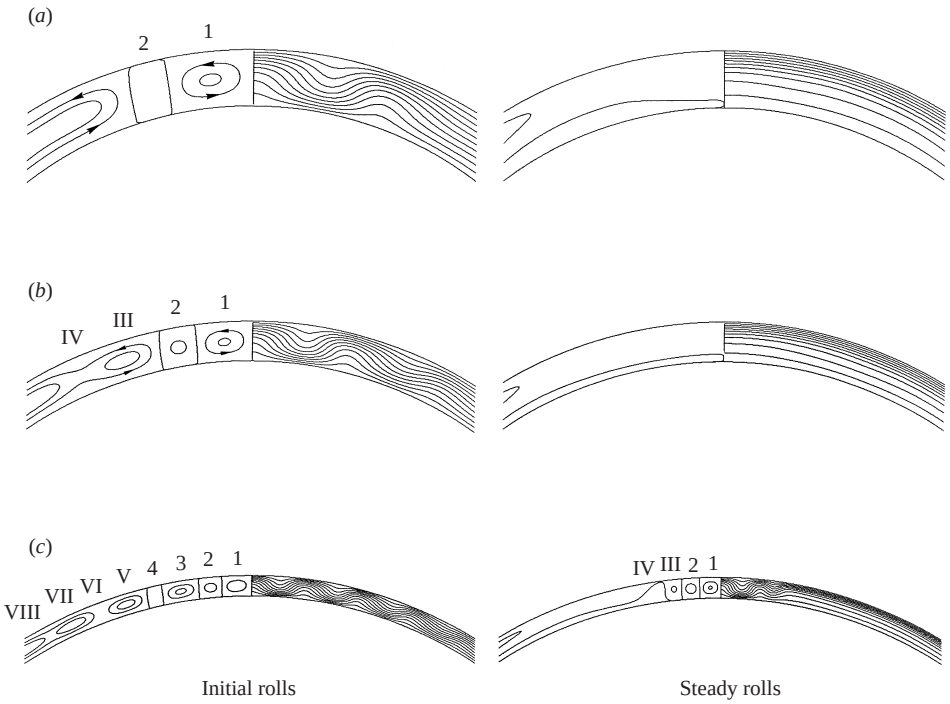

FIGURE 16. Effect of R on convection at the upper portion of the mid-axial plane for the second type of longitudinal roll pattern (upward radial velocity at $\phi = 0$) for $A = 7$, $Ra = 2500$, $Pr = 0.7$, with streamlines on the left-hand sides and isotherms on the right-hand sides for initial rolls and steady rolls: (*a*) $R = 1.15$; (*b*) $R = 1.1$; (*c*) $R = 1.05$.

as observed in figure 16(*c*). It is evident from these results that an even number of longitudinal rolls is always present on each side of the annulus for the second type of longitudinal roll pattern. This occurs since the uppermost roll and the roll adjoining the main flow rotate in opposite directions, which is possible only for an even number of counter-rotating rolls. It is also seen that the second type of longitudinal roll pattern becomes established at steady state for annulus radius ratios less than a critical value R_2, where $1.05 < R_2 < 1.1$. If $R > R_2$, the transverse rolls displace the longitudinal rolls at steady state. Note that steady state overall Nusselt numbers for the first and second types of longitudinal roll patterns were compared to each other for the case of $R = 1.05$ and $Ra = 2500$, and found to be essentially the same.

The angular extent of the fully and partially separated longitudinal rolls present early-on for $Ra = 2500$ remained within approximately $\pm 30^\circ$ over the range of R studied. This can be clearly seen by examining the streamlines and the alternating elevation and depression of isotherms plotted on the left-hand sides of figures 15 and 16. There are, of course, a greater number of rolls for smaller R since the gap thickness is reduced and more rolls of approximately the same aspect ratio can fit into the same angular region. At steady state conditions, the angular extent of the fully and partially separated longitudinal rolls is reduced to within approximately $\pm 10^\circ$ for the range of R studied as a result of the formation of transverse rolls, as seen on the right-hand sides of figures 15(*b*), 15(*c*) and 16(*c*). This approximate boundary between longitudinal and transverse rolls agrees well with the experimentally determined critical angle of inclination for a rectangular box of 9° reported by Kirchartz &

Oertel (1988). Below this critical angle, rolls oriented perpendicular to the basic flow in the box (corresponding to longitudinal rolls in the annulus) arise as Ra is increased above Ra_c. As the angle of inclination is increased above the critical value, rolls oriented parallel to the basic flow (corresponding to transverse rolls in the annulus) become established.

As clearly seen in the streamline plots provided on the left-hand sides of figures 13(*b*), 13(*c*), 15(*b*), 15(*c*) and 16(*a*)–16(*c*), and on the right-hand side of figure 16(*c*) (all corresponding to when more than one fully separated longitudinal roll is in place on each side of the annulus), the longitudinal rolls that rotate in the same direction as the main flow (like-rotating) are stronger than the adjoining longitudinal rolls that rotate in the opposite direction (opposite-rotating). Within the like-rotating rolls, the fluid moves upward along the positively inclined inner cylinder wall as it is heated and downward along the negatively sloping outer cylinder wall as it is cooled, and thus the flow along the walls is aided by buoyancy forces. Within the opposite-rotating rolls, however, the fluid moves in the opposite directions along the cylinder walls in local opposition to buoyancy forces. Therefore, owing to the slope of the cylinder walls, the like-rotating rolls are stronger. The strength of the like- and opposite-rotating longitudinal rolls is seen to decrease and increase, respectively, with decreased distance from the top of the annulus. This occurs as a result of the decreasing slope of the cylinder walls and the corresponding reduction in the influence of wall inclination on roll strength just described. These results indicate that at a given Rayleigh number, the strength of a longitudinal roll is dependent both on its direction of rotation and its location relative to the top the annulus.

An overall representation of the orientations and numbers of steady convective rolls associated with the four different convective states investigated in the present work is provided in figure 17 for $R = 1.05$, $A = 7$ and $Ra = 2500$. Schematic diagrams of the boundaries of the convective rolls present in the upper portion of the annulus are shown in figure 17 for each state. The view is from above the annulus looking downward. In figures 17(*a*) and 17(*b*), it can be seen that the first and second types of transverse roll patterns exhibit six transverse rolls ($T1$–$T6$) in the upper region of the annulus. The directions of rotation of the rolls in figure 17(*a*) are opposite to those of the corresponding rolls in figure 17(*b*). Note that the figure 17(*a*) schematic corresponds to the results shown in figure 9 for $R = 1.05$. In figure 17(*c*), it can be seen for the first type of longitudinal roll pattern that two fully separated longitudinal rolls (1, 4) (accompanied by four counter-rotating regions (II, III, V, VI)) separate six transverse rolls on one side of the annulus ($T1$–$T6$) from six transverse rolls on the other side of the annulus ($T7$–$T12$). In figure 17(*d*) for the second type of longitudinal roll pattern, four fully separated longitudinal rolls (1, 2, 5, 6) (accompanied by four counter-rotating regions III, IV, VII, VIII) separate six transverse rolls on one side of the annulus ($T1$–$T6$) from six transverse rolls on the other side of the annulus ($T7$–$T12$). The longitudinal rolls in figure 17(*c*) rotate in the opposite directions of the corresponding longitudinal rolls in figure 17(*d*). The transverse rolls in figure 17(*c*) ($T1$–$T12$) rotate in the same directions as the corresponding transverse rolls in figure 17(*d*). It is noted that the figure 17(*c*) and 17(*d*) schematics correspond to the results shown on the right-hand sides of figure 15(*c*) and 16(*c*), respectively.

4. Conclusions

An investigation of three-dimensional buoyancy-driven flow in a narrow-gap annulus has been performed for the first time. It was shown that in a narrow-gap

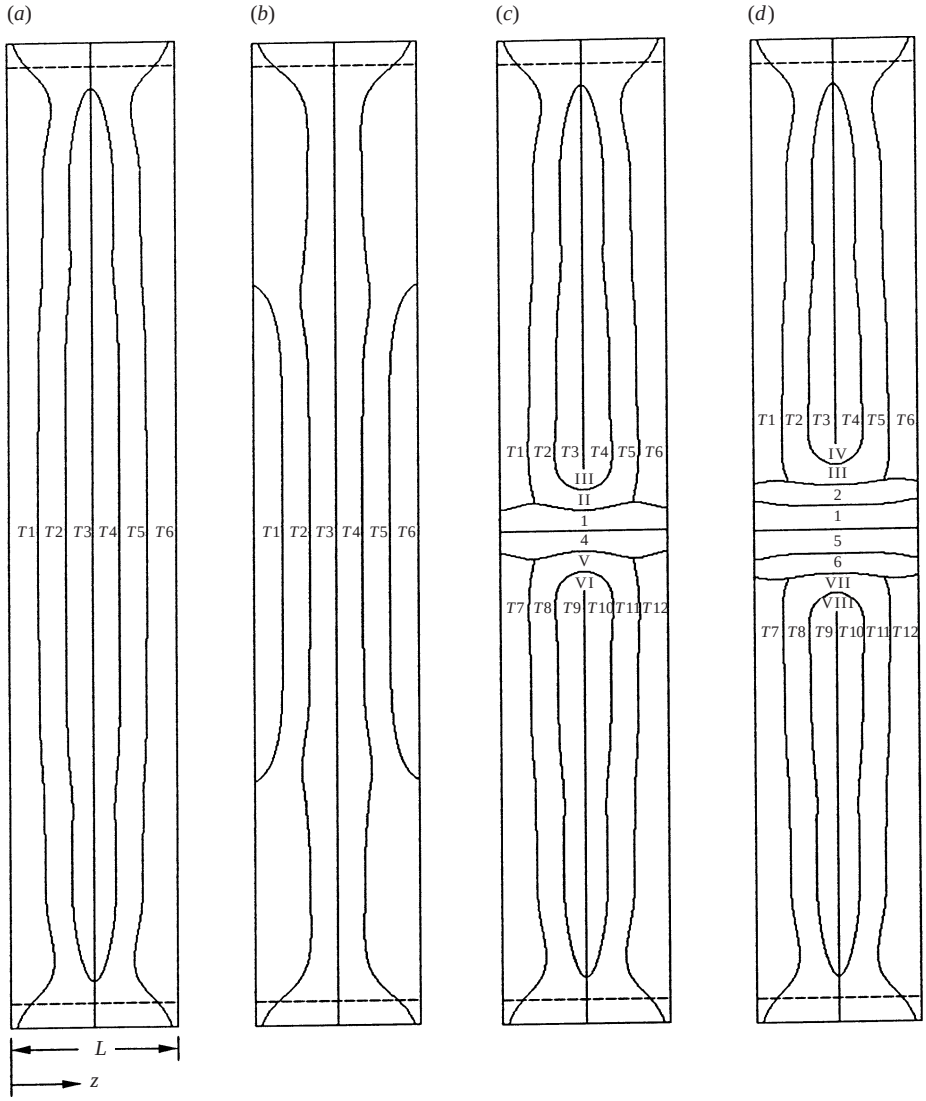

FIGURE 17. Boundaries of the steady convective rolls in the upper portion of the annulus (as viewed from above the annulus looking downward) for $R = 1.05$, $A = 7$, $Ra = 2500$ and $Pr = 0.7$: (*a*) first type of transverse roll pattern; (*b*) second type of transverse roll pattern; (*c*) first type of longitudinal roll pattern; (*d*) second type of longitudinal roll pattern.

annulus with impermeable endwalls, the onset of thermal instabilities leads to the development of three-dimensional flow in the upper portion of the annulus consisting of multiple counter-rotating rolls. Four different supercritical states that have not been previously identified for narrow-gap annuli were examined in detail for air. The structure of three-dimensional subcritical flow, and two-dimensional supercritical flow occurring early in the transient development of the flow field were also investigated.

At low Rayleigh numbers, the flow in a narrow-gap annulus is similar to that in annuli with larger R, with two-dimensional crescent-shaped patterns present in the core region and a three-dimensional rotational structure located in the upper portion of the annulus at each endwall. When the Rayleigh number is successively increased

from a subcritical value to above Ra_c, however, an integral number of transverse roll pairs forms between the existing end rolls owing to thermal instability (similar to that in a moderate-gap annulus), resulting in the first supercritical state. An analysis was conducted which showed that when the inception of instability occurs prior to the development of the end rolls, three additional supercritical states (one described in § 3.1, and the other two in § 3.2) can occur. Each of the four supercritical states exhibits either transverse rolls or a combination of longitudinal and transverse rolls in the upper portion of the annulus.

Two types of steady supercritical states exhibiting only transverse rolls in the upper region of a narrow-gap annulus were investigated. The first type is characterized by end rolls that rotate clockwise and counterclockwise on the right- and left-hand sides of the annulus, respectively. The second type has the same number of transverse rolls as the first type, but with reversed directions of rotation. Accordingly, the second type is characterized by end rolls that rotate counterclockwise and clockwise on the right- and left-hand sides of the annulus, respectively. It was found that the second type of supercritical state bifurcates from the first type at a Rayleigh number greater than Ra_c. The transverse rolls were shown to produce individual recirculating zones in which complex interactions between either one or two rolls and the primary flow take place. The fluid in the upper portion of the rolls does not interact appreciably with the main flow, which differs from the interaction between spiral vortices and the main flow that occurs in a moderate-gap annulus. It was shown that for a fixed Rayleigh number and gap aspect ratio A, the number of transverse rolls remained constant and the dimensionless strength of the rolls was nearly unchanged over the range of narrow-gap R studied. The temperature field and the inner and outer cylinder Nusselt number distributions in the upper part of the annulus were shown to be significantly affected by the transverse rolls.

Two types of supercritical states exhibiting longitudinal rolls in the top portion of the annulus in combination with transverse rolls between the longitudinal rolls and the main flow were studied. The first type is characterized by uppermost longitudinal rolls with a downward radial velocity at the upper vertical angular plane, and has an odd number of longitudinal rolls on each side of the annulus. This type was found to set up in annuli with a radius ratio R less than a critical value R_1, where $1.1 < R_1 < 1.15$. The second type displays uppermost rolls with an upward radial velocity at the upper vertical angular plane (rolls with reversed directions of rotation) and has an even number of longitudinal rolls on each side of the annulus. This type arises in annuli with R less than a second critical value R_2, where $1.05 < R_2 < 1.1$. The angular extent of the steady longitudinal rolls associated with each of these two states remained within approximately $\pm 10^\circ$ of the top of the annulus. The three-dimensional flow structures in regions of the annulus below the longitudinal rolls were found to be essentially the same as for the first type of supercritical state involving only transverse rolls, consisting of individual recirculating zones involving the transverse rolls and the primary flow. Again, it was found that the fluid in the longitudinal rolls does not interact appreciably with the main flow. The temperature field and the inner and outer cylinder Nusselt number distributions at the top of the annulus are significantly affected by the longitudinal rolls.

It was shown that at early times in the transient development of the flow field, two-dimensional flow consisting only of longitudinal rolls can arise in the upper portion of the annulus owing to thermal instability. These initial longitudinal rolls, which correspond to the multiple counter-rotating cells considered in previous two-dimensional studies, persist undiminished until transverse rolls begin to form at a

later time. At sufficiently high Rayleigh numbers and for sufficiently small R, the flow then transitions to one of the two final three-dimensional supercritical states exhibiting longitudinal rolls in combination with transverse rolls. Both the number and angular extent of the fully separated initial longitudinal rolls are greater than for the subsequent fully separated steady longitudinal rolls. The number of fully separated initial longitudinal rolls tends to increase with either higher Rayleigh number or decreased R, and the angular extent of these rolls increases with higher Rayleigh number.

REFERENCES

Bishop, E. H. & Carley, C. T. 1966 Photographic studies of natural convection between concentric cylinders. *Proc. Heat Transfer Fluid Mech. Inst*. 63–78.

Brian, P. L. T. 1961 A finite difference method of high-order accuracy for the solution of three-dimensional transient conduction problems. *AIChE J*. **7**, 367–370.

Cadiou, P., Desrayoud, G. & Lauriat, G. 1998 Natural convection in a narrow horizontal annulus: the effects of thermal and hydrodynamic instabilities. *Trans. ASMEC: J. Heat Transfer* **120**, 1019–1026.

Cheddadi, A., Caltagirone, J. P., Mojtabi, A. & Vafai, K. 1992 Free two-dimensional convective bifurcation in a horizontal annulus. *Trans. ASMEC: J. Heat Transfer* **114**, 99–106.

Chung, J. D., Kim, C.-J., Yoo, H. & Lee, J. S. 1999 Numerical investigation on the bifurcative natural convection in a horizontal concentric annulus. *Numer. Heat Transfer* A **36**, 291–307.

Desai, C. P. & Vafai, K. 1994 An investigation and comparative analysis of two- and three-dimensional turbulent natural convection in a horizontal annulus. *Intl J. Heat Mass Transfer* **37**, 2475–2504.

Dyko, M. P., Vafai, K. & Mojtabi, A. K. 1999 A numerical and experimental investigation of stability of natural convective flows within a horizontal annulus. *J. Fluid Mech.* **381**, 27–61.

Fant, D. B., Prusa, J. & Rothmayer, A. 1990 Unsteady multicellular natural convection in a narrow horizontal cylindrical annulus. *Trans. ASMEC: J. Heat Transfer* **112**, 379–387.

Fant, D. B., Rothmayer, A. & Prusa, J. 1991 Natural convective flow instability between horizontal concentric cylinders. *J. Thermophys. Heat Transfer* **3**, 407–414.

Fusegi. T. & Farouk, B. 1986 A three-dimensional study of natural convection in the annulus between horizontal concentric cylinders. *Proc. 8th Intl Heat Transfer Conf*. vol. 4, pp. 1575–1580.

Grigull, U. & Hauf, W. 1966 Natural convection in horizontal cylindrical annuli. *Proc. 3rd Intl Heat Transfer Conf*. vol. 2, pp. 182–195.

Hirasaki, G. J. & Hellums, J. D. 1968 A general formulation of the boundary conditions on the vector potential in three-dimensional hydrodynamics. *Q. Appl. Maths* **26**, 331–342.

Kim, C.-J. & Ro, S. T. 1994 Numerical investigation on bifurcative natural convection in an air-filled horizontal annulus. *Proc. 10th Intl Heat Transfer Conf*. vol. 7, pp. 85–90.

Kirchartz, K. R. & Oertel jr, H. 1988 Three-dimensional thermal cellular convection in rectangular boxes. *J. Fluid Mech.* **192**, 249–286.

Kuehn, T. H. & Goldstein, R. J. 1976 An experimental and theoretical study of natural convection in the annulus between horizontal concentric cylinders. *J. Fluid Mech.* **74**, 695–719.

Liu, C., Mueller, W. K. & Landis, F. 1961 Natural convection heat transfer in long horizontal cylindrical annuli. *International Developments in Heat Transfer*, part V, pp. 976–984.

Powe, R. E., Carley, C. T. & Bishop, E. H. 1969 Free convective flow patterns in cylindrical annuli. *Trans. ASMEC: J. Heat Transfer* **91**, 310–314.

Rao, Y. F., Miki, Y., Fukuda, K., Takata, Y. & Hasegawa, S. 1985 Flow patterns of natural convection in horizontal cylindrical annuli. *Intl J. Heat Mass Transfer* **28**, 705–714.

Takata, Y., Iwashige, K., Fukuda, K. & Hasegawa, S. 1984 Three-dimensional natural convection in an inclined cylindrical annulus. *Intl J. Heat Mass Transfer* **27**, 747–754.

Vafai, K. & Ettefagh, J. 1991 An investigation of transient three dimensional buoyancy driven flow and heat transfer in a closed horizontal annulus. *Intl J. Heat Mass Transfer* **34**, 2555–2570.

WALTON, I. C. 1980 The stability of free convection in a horizontal cylindrical annulus. *Q. J. Mech. Appl. Math.* **33**, 125–139.

YOO, J.-S. 1996 Dual steady solutions in natural convection between horizontal concentric cylinders. *Intl J. Heat Fluid Flow* **17**, 587–593.

YOO, J.-S., CHOI, J. Y. & KIM, M.-U. 1994 Multicellular natural convection of a low Prandtl number fluid between horizontal concentric cylinders. *Numer. Heat Transfer* A **25**, 103–115.